https://doi.org/10.5194/egusphere-2026-5232
Preprint. Discussion started: 11 September 2026


# A mosaic of aerosol sources in the central Mediterranean: insights from dry deposition and single-particle analyses

Marcos Morán[1], Kilian Schneiders[1], Melanie Eknayan[1], Ferdinando De Tomasi[2], Pierina Ielpo[3], Mark Scerri[1,4], Michael Nolle[5], and Konrad Kandler[1]

[1]Institute for Applied Geosciences, Technical University Darmstadt, 64287 Darmstadt, Germany
[2]University of Salento, Department of Mathematics and Physics, 73100 Lecce, Italy
[3]Institute of Atmospheric Sciences and Climate, Italian National Research Council (CNR ISAC), 73100 Lecce, Italy
[4]Division of Environmental Management & Planning, Institute of Earth Systems, University of Malta, MSD 2080 Msida, Malta
[5]Ambient Quality Unit, Environment and Resources Authority, MRS 1441 Marsa, Malta

**Correspondence:** Marcos Morán (moran@geo.tu-darmstadt.de) and Pierina Ielpo (pierina.ielpo@cnr.it)

**Abstract.** Flux-based dry deposition observations are scarce in the central Mediterranean, leaving unresolved how transport shapes deposited composition. Dry deposition was sampled concurrently at Lecce, southern Italy, and San Lawrenz, Malta, from spring 2017 to winter 2018 within the XMed-Dry network, using flat-plate collectors with 48–72 h exposures. Up to 5000 particles per sample were classified by scanning electron microscopy with X-ray fluorescence, and source regions were derived from FLEXPART backward simulations weighted first by hourly $PM_{10}$ and then by class-resolved deposition rates. Mineral dust dominated the deposited mass in 95 % of samples at inland Lecce but 69 % at coastal San Lawrenz, where the sea-salt flux was an order of magnitude higher. Dust sources peaked over northern Algeria and Tunisia at Lecce but over Libya at San Lawrenz, and sea salt at Lecce reached the northeastern Atlantic, increasingly with size, while at San Lawrenz it remained within the western Mediterranean. Intensity instead separates the classes. The five strongest events carried about 20 % of the dust mass at both sites but 40 % of the sulfate mass. Within several intrusions, silicate-sulfate and silicate-sea-salt mixtures peaked after the dust maximum, indicating progressive processing as the event decayed, and these episodes carried higher iron proportions across all size fractions. Such processing reportedly raises iron solubility, increasing bioavailable iron delivered to surface waters. Mineral classes intercorrelate strongly except Ca-rich particles, whose mass at San Lawrenz held through boreal winter, when Saharan input reached its seasonal minimum, indicating a local carbonate source.

## 1 Introduction

Aerosol dry deposition is a fundamental process through which particles are transferred from the atmosphere to Earth's surface in the absence of precipitation (Connan et al., 2018; Emerson et al., 2020; Pacyna, 2008; Thiagarajan et al., 2024). As part of the broader aerosol cycle, it plays a central role in regulating atmospheric composition by acting as a major sink that shortens aerosol lifetimes and shapes their spatial distribution (Emerson et al., 2020; Farmer et al., 2021; Wu et al., 2018a). The efficiency of this removal pathway is controlled by meteorological conditions and particle properties, most notably the interplay between turbulence, Brownian motion, and gravitational settling, which together determine how particles of different

https://doi.org/10.5194/egusphere-2026-5232
Preprint. Discussion started: 11 September 2026


sizes are transported to the surface and removed from the atmosphere (Connan et al., 2018; Farmer et al., 2021; Farmer and Riches, 2020). While wet deposition often dominates aerosol removal in regions with frequent precipitation, dry deposition can become the primary sink under cloud-free conditions and has accounted for around 50 % of particulate mass removal in some observational studies (Wu et al., 2018b). Dry deposition influences radiative forcing, atmospheric chemistry, and the delivery of nutrients and pollutants to terrestrial and marine ecosystems, therefore accurately quantifying this process remains essential for understanding its implications for climate, air quality, and ecological dynamics (Cui et al., 2010; Emerson et al., 2020; Lin et al., 2019; Mahowald et al., 2017; Varenik and Konovalov, 2021). For example, Mahowald et al. (2017) estimated that enhanced nutrient inputs from atmospheric deposition increase terrestrial carbon uptake across ecosystems by 0.2–1.5 Pg C $yr^{-1}$.

In this context, the Mediterranean lies at the intersection of several major atmospheric transport pathways, making it a region where contrasting air-mass influences frequently converge (Dayan, 2023b; Dulac et al., 2023; Kaskaoutis et al., 2023). Westerly flows from the North Atlantic, southerly intrusions from the Sahara, and continental outflows from southeastern Europe and the eastern Mediterranean all periodically reach the basin, delivering distinct atmospheric fluxes that shape its aerosol environment (Adame et al., 2022; Bibi et al., 2020; Chiapello et al., 2021; Dimitriou et al., 2022a; Floutsi et al., 2016; Schepanski et al., 2016). The relative importance of these pathways varies across subregions of the Mediterranean, with western, central, and eastern sectors each exhibiting characteristic circulation patterns and seasonal regimes (Bibi et al., 2020; Dimitriou et al., 2022a; Floutsi et al., 2016). These spatial and temporal contrasts highlight the importance of large-scale circulation for interpreting dry deposition within the basin.

However, how such circulation variability translates into the material ultimately delivered to the surface remains poorly understood. In the central Mediterranean in particular, long-term deposition measurements are scarce, and most available studies rely on atmospheric concentrations rather than flux-based observations, providing limited insight into the composition and variability of deposited material (Vincent et al., 2016). As a result, it remains unclear how different air-mass trajectories influence surface loading or how mixtures of marine, desert-derived, and continental inputs are represented in the deposition record. This lack of observational constraints limits efforts to evaluate dry-deposition processes in one of the most dynamically complex sectors of the Mediterranean basin.

Addressing these limitations requires observational strategies capable of capturing both the magnitude of dry deposition and the diversity of atmospheric inputs that contribute to it. This, in turn, calls for deposition measurements collected under contrasting transport conditions, together with analytical approaches that can resolve the single-particle characteristics of the deposited material. Equally essential is the integration of deposition observations with air-mass histories, enabling the pathways that deliver material to the surface to be linked to the attributes of what is ultimately deposited. Such a combined framework provides the basis for advancing process-level understanding of deposition in regions shaped by complex and variable circulation.

To contribute to this effort, the present study draws upon a multi-season series of dry deposition samples collected concurrently at two sites in the central Mediterranean—Lecce in southern Italy and San Lawrenz on the island of Gozo, Malta—from spring 2017 to winter 2018. The overlapping sampling period permits a parallel examination of deposition within a shared

https://doi.org/10.5194/egusphere-2026-5232
Preprint. Discussion started: 11 September 2026


regional setting. Deposition flux measurements are combined with single-particle analyses of the deposited material to characterize its compositional diversity, while backward modelling of air masses identifies the transport pathways and source regions associated with each sampling interval. Integrating these components enables the assessment of how marine, desert-derived, and continental inputs are expressed in surface deposition across the two locations. In this way, the study provides new insight into the processes governing dry deposition in one of the most dynamically complex sectors of the Mediterranean basin.

## 2 Data and Methods

### 2.1 Field Campaign

As a first step in the present study, dry deposition samples were collected at two strategic locations in the central Mediterranean: the Ecotekne Campus in Lecce, southern Italy (18°06' E, 40°20' N; 40 m above sea level), and the coastal site of San Lawrenz on Gozo Island, Malta (14°12' E, 36°03' N; 130 m above sea level). These two stations, separated by approximately 585 km along a NE–SW transect, form part of the XMed-Dry network, a coordinated observational campaign established to quantify atmospheric deposition across a series of Mediterranean and eastern Atlantic environments (Kandler et al., 2018a; Rizza et al., 2021). The overarching aim of XMed-Dry is to generate harmonized dry deposition datasets from sites influenced by contrasting meteorological regimes and air-mass pathways, thereby enabling region-wide assessments of deposition variability and its driving processes.

Although the full network includes several stations distributed across Spain, France, Malta, Italy, Greece, and Cyprus (Kandler et al., 2018a), the present work focuses exclusively on the samples obtained in Lecce (LES) and San Lawrenz (SLS). These two sites offer overlapping multi-season time series from spring 2017 to winter 2018, providing a coherent temporal window for direct comparison. The simultaneous availability of samples, summarized in Figure 1, ensures consistency in evaluating seasonal behavior and event-scale variability in deposition.

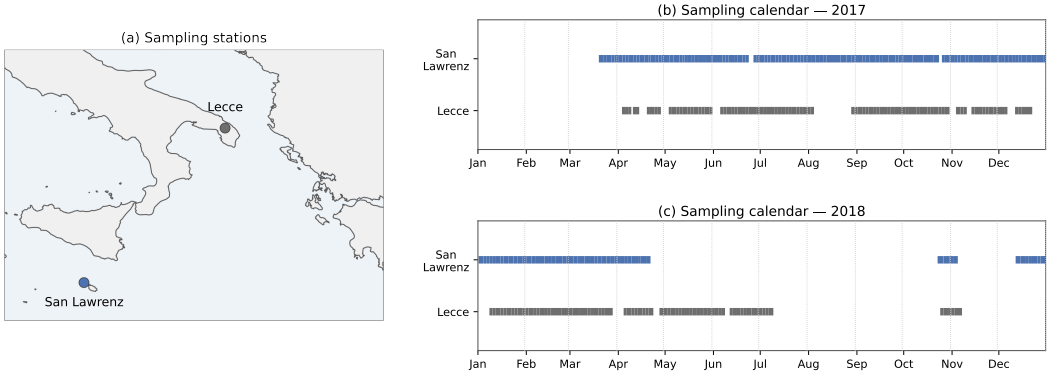


**Figure 1.** Sampling calendar and station location, which continuous bars are sampling periods made up of consecutive samples and gaps are periods without a valid sample.

https://doi.org/10.5194/egusphere-2026-5232
Preprint. Discussion started: 11 September 2026


Dry deposition was collected using samplers based on a modified flat-plate geometry (Waza et al., 2019), which laminarizes the atmospheric flow between two parallel plates (Figure 2) and thereby promotes reproducible particle deposition onto the sampling substrate.

**Figure 2.** Dry deposition collector. In the top part is an actuator, which lowers the outermost section in case of rain to protect the lower plate of the collector from rain. Rain is detected by an infrared rain sensor.

To prevent contamination by wet deposition, in addition to the setup described by Waza et al. (2019), the configuration included an active rain-protection mechanism triggered by an infrared rain detector. When rainfall is detected, an actuator mounted above the top plate lowers the external section of the top plate, shielding the substrate from incoming droplets. In addition to this active protection, the sampler geometry itself provides a passive rain shield: the larger upper plate and smaller lower plate reduce the likelihood of droplet intrusion, particularly under low wind speeds or for larger droplets.

The sampling head was installed approximately 2 m above rooftop level to minimize the influence of local surface effects (Kandler et al., 2018a; Rizza et al., 2021). Individual samples were exposed for 48–72 hours and subsequently stored in sealed containers under dry conditions at room temperature until further analysis (Rizza et al., 2021).

Particles were collected on 25 mm pure carbon adhesive tabs (SpectroTabs, Plano GmbH, Wetzlar, Germany) mounted on aluminum stubs and stored in plastic boxes at room temperature prior to microscopic analysis.

## 2.2 Single-particle electron microscopy analysis

### 2.2.1 SEM–XRF particle detection and quantification

Deposited particles were characterized using automated scanning electron microscopy (SEM; FEI Quanta 400F ESEM, FEI, Eindhoven, The Netherlands) coupled with X-ray fluorescence spectroscopy (XRF; Oxford X-Max 120, Oxford Instruments, Abingdon, UK) under high-vacuum conditions. Prior to further analysis, samples were visually inspected by SEM in order to exclude damaged surface regions or areas affected by droplet deposition.

https://doi.org/10.5194/egusphere-2026-5232
Preprint. Discussion started: 11 September 2026


Automated image acquisition was then performed on randomly selected analysis fields at a spatial resolution of 100–150 nm per pixel. Particle detection was achieved through image segmentation based on backscattered electron contrast, which allowed particles to be distinguished from the substrate. The identified particles were subsequently analyzed using an automated XRF system. Image acquisition and particle analysis were repeated until either 5000 particles were analyzed per sample or a maximum analysis time of 12 h was reached. Further details on data acquisition, quantification, and processing are provided elsewhere (Kandler et al., 2018b; Waza et al., 2019).

Particle size metrics were derived from the particle morphology observed in the SEM images. The projected-area diameter was obtained from the projected cross-sectional area of each particle. Following the approach of Kandler et al. (2018b) and Ott et al. (2008), the volume-equivalent diameter was calculated from the particle perimeter and therefore accounts for particle shape. Particle mass was estimated from the volume-equivalent diameter using a simplified density model assuming a density of 2650 kg $m^{-3}$ for dust particles and 2200 kg $m^{-3}$ for non-dust compounds.

XRF acquisition times were adjusted to obtain at least 50 000 X-ray counts per particle. During analysis, the electron beam scanned the particle cross section while the integrated X-ray spectrum was recorded. Elemental quantification was performed using Oxford Aztec software (versions 4.0–6.2), yielding weight-percentage compositions for the analyzed particle volume. Although elements with atomic number $Z > 4$ could in principle be quantified, only elements with $Z > 8$ were considered for the data analysis due to substrate contributions and large uncertainties associated with light elements.

In a considerable number of particles, small amounts of Pb were quantified by the quantification software. As the Pb M line transitions are colocated with the S K lines, this quantification can be influenced by noise in the spectrum. To corroborate the existence of Pb, we therefore checked the backscatter electron image brightness for the according particles and compared it to the average brightness of similarly-composed particles (ignoring the Pb). We found that for the same particle size, the image brightness increases on average with the quantified Pb content (Fig. S1 and S2 in the electronic supplement). We therefore treat the detection of Pb as reliable.

Particles intersecting the edge of an analysis field were excluded because their size cannot be reliably determined. Since this procedure reduces the effective analysis area for larger particles, a particle-specific weighting factor (window correction) was applied to compensate for the decreasing sampling area with increasing particle size (Kandler et al., 2009).

### 2.2.2 Blank and contamination correction

Blank correction is often not required in SEM-based particle analyses (Axson et al., 2016; Kandler et al., 2020, 2018b) because particle concentrations on sampling substrates typically exceed blank levels by several orders of magnitude. In the present study, however, aerosol concentrations varied substantially and included periods of very low deposition, which resulted in particle densities low enough to require a blank correction. For this reason, to quantify background contamination, 26 laboratory and handling blank substrates from different charges were analyzed using the same SEM–XRF procedure as for the samples, but covering a larger fraction of the substrate surface to allow for higher contamination particle numbers. For each particle type (see Section 2.2.3), particle number densities per unit area were determined.

https://doi.org/10.5194/egusphere-2026-5232
Preprint. Discussion started: 11 September 2026


The limit of detection was defined as the upper bound of the central 90 % confidence interval ($\alpha = 0.95$) of the blank particle number densities. When the particle number density of a given type in a sample exceeded this limit, particles were assigned a reduced counting weight according to:

$$W_{\mathrm{blank}} = 1 - \frac{N_{\mathrm{blank}}}{N_{\mathrm{sample}}} \tag{1}$$

where $N_{\mathrm{blank}}$ and $N_{\mathrm{sample}}$ represent the particle number densities for each particle type on the mean blank and on the respective sample.

In addition to the blank correction, particles with compositions resembling silicon–fluorine, stainless steel, brass, aluminum–chlorine, and aluminum–copper–silver compounds were completely excluded from the analysis, as their atmospheric origin on the sample is highly questionable. The overall fraction of contamination particles was nevertheless small (2 % of all analyzed particles). Of these, 87 % consisted of silicon–fluorine compounds, most likely associated with the anti-adhesive treatment of the release liner of the carbon adhesive tabs.

### 2.2.3 Particle classification scheme

Several classification schemes exist for single-particle measurements based on elemental compositions derived from energy-dispersive X-ray spectroscopy (EDS) analysis, ranging from unsupervised machine-learning approaches (e.g., cluster analysis) to predefined decision-tree or rule-based schemes (Kandler et al., 2018b). In this study, a compositional-similarity approach was adopted, in which measured particle compositions were compared to a predefined set of potential compositions representing different particle types. In addition, a non-hierarchical Gaussian mixture cluster analysis based on elemental compositions was applied to identify particle types not included in the initial definition. This procedure revealed an additional class of sulfate-mixture particles. Because chemical similarity between a measured particle composition and a mineral composition does not necessarily imply that the particle consists of that mineral, particle-type nomenclature includes the suffix "–like". This discrepancy arises mainly from two factors. First, some minerals, particularly common silicates, exhibit overlapping elemental compositions. Second, the EDS measurement yields an average composition for each particle, which may represent mixtures of different mineral phases. Both limitations are inherent to the measurement technique.

A complete table of the classification definitions is provided in the Table S1 of the supplement. Using normalized atomic contributions of the elements F, Na, Mg, Al, Si, P, S, Cl, K, Ca, Ti, Cr, Mn, Fe, Ni, Cu, Sr, Zr, Ag, Ba, and Pb, we define a 21-dimensional elemental space. Within this space, reference points are defined for potential particle compositions. Typically, one reference composition represents a particle group, although multiple compositions may be used for groups with variable chemistry (e.g., pyroxene/amphibole-like particles or complex sulfate mixtures). These particle groups are further aggregated into broader particle classes (e.g., silicates or soluble sulfates), which are subsequently grouped into aerosol types such as sea salt, sulfates, or mineral dust.

The similarity between a measured particle composition and a reference composition is quantified using the normalized Euclidean distance in the elemental space. Each particle is assigned to the group with the smallest distance. For comparison,

https://doi.org/10.5194/egusphere-2026-5232
Preprint. Discussion started: 11 September 2026


also the maximum (city-block) norm has been used; however, the resulting classifications differed only negligibly. For the Euclidean distance, the normalization factor is $\sqrt{2}$, whereas for the maximum norm it is 2, corresponding to the maximum possible distance in the normalized space.

Compared with element-concentration or element-ratio rule-based classification schemes, this approach offers mainly two advantages. First, the distance metric provides a quantitative quality criterion, allowing particles with insufficient similarity to any reference composition to be assigned to an unclassified category. In addition, the method avoids overlaps between classification rules by implicitly defining 21-dimensional polyhedra around each reference composition. Such overlaps can be difficult to resolve, if many elemental contributions are considered simultaneously.

Note that small differences between similar reference compositions should not necessarily be considered significant, even if the full classification table might suggest otherwise. Nevertheless, a complete set of potential compositions is necessary to avoid leaving regions of the element space unassigned, which would increase the risk of misclassification.

#### 2.2.4 Uncertainty estimation of deposition rates

Under the assumption of a perfectly homogeneous particle distribution on the substrate, the uncertainty of number-based deposition rates could be approximated by a Poisson distribution, whereas uncertainties in mass-based deposition rates would require simulation approaches such as bootstrap resampling (Kandler et al., 2018b). In practice, however, particle deposition on the substrates is not perfectly homogeneous. The factors that contribute to this heterogeneity include imperfect substrate smoothness, flow distortion by the deposition of very large particles or plant debris, droplet deposition, and surface defects. During the quality screening procedure, obvious defects, plant debris, and areas affected by droplet deposition were excluded from the analysis. Nevertheless, the imperfect smoothness and the influence of very large particles are inherent to the sampling method and lead to local variations in deposition concentration due to small differences in airflow exposure.

In principle, local variability could be assessed using a bootstrap approach based on analysis fields, if a sufficient number of fields is available. In this study dataset, however, dust concentrations varied strongly. For samples with high particle concentrations, only a small number of analysis fields reach the target particle number, preventing a statistically meaningful field-based bootstrap analysis. Therefore, a particle-based approach using Voronoi tessellation (Okabe et al., 1992) was adopted. The analyzed area was divided into polygons surrounding each particle, with polygon size varying based on the local particle deposition density. Because analysis fields are spatially separated, each field was treated independently. Voronoi polygons located at the outer boundary of a particle set would theoretically extend to infinity. To avoid this, polygon boundaries were constrained by the edges of the analysis fields. This was achieved by mirroring particle coordinates across each field boundary, resulting in Voronoi polygons with straight edges along the field borders. As a result, this process assigns a variable area per particle with lower areas in regions of higher concentration and vice versa.

A standard bootstrap procedure (Efron, 1979; Kandler et al., 2018b) with 9999 replications was then applied to estimate number- and mass-based deposition rates for each sample. Because deposition rates are defined as the sum of particle numbers or masses per analysis area and exposure time, each bootstrap replicate was multiplied by the inverse of the total area associated with the particles selected in that replicate. This procedure effectively simulates the random sampling of regions

https://doi.org/10.5194/egusphere-2026-5232
Preprint. Discussion started: 11 September 2026


with different particle densities and therefore accounts for spatial variability in deposition. As expected, the approach yields larger uncertainties for samples exhibiting stronger spatial heterogeneity in particle deposition. All statistical and geometrical analyses were performed using the Python library SciPy version 1.15.2 (Virtanen et al., 2020).

### 2.3 Potential Source Regions Identification

To identify the potential source regions contributing to the particle types observed in the dry-deposition samples, a backward air-mass modelling framework was applied using the FLEXPART Lagrangian dispersion model (version 11) (Bakels et al., 2024). FLEXPART provides three-dimensional residence-time fields (sensitivity) that describe the upwind locations where air parcels spent time before reaching the receptor sites.

Based on this transport information, a two-step Concentration Weight Trajectory (CWT) analysis was carried out. In the first step, hourly $PM_{10}$ concentrations at the sampling sites were used as the concentration field, because deposition rates, obtained from SEM analyses, represent multi-day integrated measurements and do not resolve sub-daily variability. Therefore, using $PM_{10}$ as a proxy enables a temporally refined estimation of general source influences. In the second step, deposition rates (mg $m^{-2}$ $d^{-1}$) were used directly as the concentration term, allowing the attribution of potential source regions specifically for the material that effectively reached the surface.

The following sections describe these methodological components in detail.

#### 2.3.1 Air Masses Backward Modelling

For each sample, FLEXPART was run in backward mode to quantify air-mass sensitivity at the receptor sites. Because the dry-deposition samples integrate over several days, each sampling period was subdivided into shorter segments to resolve intra-period variability. This allowed each sensitivity field to be associated with hourly $PM_{10}$ concentrations from the Copernicus Atmosphere Monitoring Service (CAMS) European air quality reanalysis during the subsequent Direct Concentration Weight Trajectories (DCWT) analysis. A temporal resolution of 3 h was adopted, resulting in multiple backward simulations per sample, depending on the exposure duration. The CAMS European air quality reanalysis dataset was employed because in situ air-quality observations at the nearest monitoring station were available only at daily frequency, whereas the characterization of diurnal variability requires concentration data with hourly temporal resolution.

To implement this framework, FLEXPART requires meteorological input fields that ensure physically consistent transport simulations. Particle motion is computed using variables interpolated in space and time from three-dimensional, grid-resolved meteorological fields, including wind components, temperature, specific humidity, cloud liquid and ice water content, as well as precipitation and selected surface-related parameters (Bakels et al., 2024). In this study, the simulations were driven by the latest European Centre for Medium-Range Weather Forecasts (ECMWF) reanalysis product, ERA5 (Hersbach et al., 2020), using hourly data at a horizontal resolution of $0.25° \times 0.25°$ across all 137 model levels. For this, the Flexextract preprocesor was used for the retrival and preparing of ECMWF data (Tipka et al., 2020), for use in a domain extended from -30° to 49.5° in longitude and from 20° to 59.5° in latitude, as shown in Figure 3.

https://doi.org/10.5194/egusphere-2026-5232
Preprint. Discussion started: 11 September 2026



**Figure 3.** Modelling domain and location of the sampling stations. Air-mass sensitivity was resolved on 33 output levels extending from the surface to 50 km above ground level.

The model configuration was designed to capture the regional-scale transport patterns and near-surface processes influencing the sampling sites. A total of 100 000 particles were released uniformly from each sampling site within a layer extending from the surface to 10 m above ground level, with releases performed at an hourly frequency, for a 5 day backward simulation period. An inert air tracer was selected as the simulated species, adopting the default tracer properties implemented in FLEXPART.

Finally, the model outputs were configured to provide gridded air-mass sensitivity fields (residence time of particles) in seconds with a temporal resolution of 1 hour and a horizontal spatial resolution of 0.125°. Likewise, vertical sensitivity was resolved at multiple discrete output levels, allowing a characterization of transport processes from the near-surface layer to the upper troposphere. Sensitivity fields were saved at heights of 0, 5, 10, 15, 20, 30, 40, 50, 75, 100, 150, 200, 250, 300, 400, 500, 600, 750, 900, 1100, 1300, 1600, 2000, 2500, 3000, 3800, 4600, 5500, 6500, 7000, 10 000, 25 000, and 50 000 meters above ground level.

### 2.3.2 Preparation of Air-Mass Sensitivity Fields for DCWT

Before applying the DCWT analysis, the raw FLEXPART sensitivity fields were pre-processed to obtain spatially consistent and physically meaningful inputs. This preparation involved three main steps: normalization by grid-cell area, integration of the sensitivity within the boundary layer, and temporal accumulation over the backward simulation period.

First, the sensitivity in each grid cell was normalized by its horizontal surface area, computed as:

https://doi.org/10.5194/egusphere-2026-5232
Preprint. Discussion started: 11 September 2026


$$A(\phi) = 193.2\ \mathrm{km}^2 \cdot \cos(\phi) \tag{2}$$

where $\phi$ is the latitude and $193.2\,\mathrm{km}^2$ is the area of one cell at the equator,

So that residence time is expressed per unit area (s $\mathrm{km}^{-2}$), removing the latitudinal distortion inherent to the model latitude–longitude grid.

Then, the normalized sensitivity was restricted to the planetary boundary layer (PBL), since this atmospheric layer governs the interaction between transported air masses and surface deposition (Li et al., 2017; Ma et al., 2024). Hourly PBL heights from ERA5 were interpolated to the FLEXPART output resolution, and sensitivity values below the PBL top were vertically integrated for each model time step.

Finally, for each deposition sample, the PBL-integrated sensitivity fields from all FLEXPART output intervals were accumulated over the 5-day backward simulation, yielding a boundary-layer sensitivity footprint used in the subsequent DCWT analyses.

### 2.3.3 Direct Concentration-Weighted Trajectories (DCWT)

The DCWT analysis provides a quantitative measure of the relative contribution, source strength, of each grid cell to the aerosol conditions observed at the receptor sites. In the classical formulation (Cheng et al., 2013; Jeong et al., 2011; Kabashnikov et al., 2011), the DCWT value for a grid cell (i,j) represents the concentration at the receptor averaged over all back trajectories. Building on the boundary-layer sensitivity fields derived in Section 2.3.2, each FLEXPART output interval was matched to the corresponding hourly $PM_{10}$ concentration at the receptor, yielding a sequence of N trajectory–concentration pairs covering the full sampling duration.

For each grid cell (i,j), the DCWT value was computed as:

$$\mathrm{DCWT}_{ij} = \mathrm{weight}_{ij} \cdot \frac{\sum_{l=1}^{N} c_l\, w_{ij,l}}{\sum_{l=1}^{N} w_{ij,l}} \tag{3}$$

where $c_l$ is the hourly $PM_{10}$ concentration at the receptor at each time step $l$, $w_{ij,l}$ is the FLEXPART air-mass sensitivity (residence time) in that cell, and the denominator reflects the total time spent by all trajectories within the cell.

Because some regions of the grid may be sparsely sampled by the trajectory ensemble, a weighting correction was introduced to reduce potential artefacts. Following the potential source contribution function (PSCF) weighting approach applied by Vratolis et al. (2023), grid cells with accumulated residence times below the 25th, 50th, and 75th percentiles were assigned weight factors of 0.25, 0.50, and 0.75, respectively, whereas cells exceeding the 75th percentile retained full weight. Although originally developed for PSCF, this weighting scheme enhances robustness in CWT applications in analogy by preventing spuriously high values in cells with very limited trajectory influence.

Finally, to facilitate visualization and comparison across samples and stations, the weighted DCWT fields were normalized by their maximum value:

https://doi.org/10.5194/egusphere-2026-5232
Preprint. Discussion started: 11 September 2026


$$\mathrm{DCWT}_{ij}^{\mathrm{norm}} = \frac{\mathrm{DCWT}_{ij}}{\max(\mathrm{DCWT}_{ij})} \tag{4}$$

The normalized DCWT values established the transport context for the subsequent Model-Assisted Concentration-Weighted Trajectories (MA-CWT).

#### 2.3.4 Model-Assisted Concentration-Weighted Trajectories (MA-CWT)

The MA-CWT extends the classical formulation by replacing both the concentration term and the trajectory weighting field with deposition-specific information. In this step, $c_l$ corresponds to the dry-deposition rate derived from SEM analysis for each particle categorization in each sample, while the weighting field $w_{ij,l}$ is taken from the normalized DCWT footprint associated with that same sample. This approach integrates the transport patterns identified in the DCWT with the magnitude and distribution of deposited material, providing a source attribution tailored to the different particle categorizations.

In this context, the MA-CWT was computed under multiple analytical configurations designed to explore complementary aspects of the deposition dataset:

- Class-specific analysis: MA-CWT maps generated separately for each SEM-defined particle class.
- Group-based analysis: Aggregated particle groups such as Pb-containing and dust.
- Seasonal analysis: Subsets defined for boreal summer and boreal winter.
- Size-resolved analysis: Deposition rates stratified by particle-size bins.

Under this formulation, grid cells exert stronger influence when (i) they consistently contributed to the air-mass transport reaching the receptor sites, and (ii) the corresponding samples exhibited elevated deposition rates for the particle category under consideration.

To limit artefacts in sparsely represented regions, a percentile-based weighting correction adapted from the DCWT was applied. For each grid cell, the number of samples with non-zero $w_{ij,l}$ values was converted into a percentile rank (1–100), and this factor (p/100) was used as a multiplicative weight. Cells frequently intersected by upwind transport retain higher weight, whereas rarely visited cells are down-weighted.

### 2.4 Complementary Analysis

As a complement to the CWT-based source attribution, additional analyses were conducted to further characterize the dry deposition dataset. Pollution-rose diagnostics were used to assess the influence of local wind conditions on deposition rate, boundary-layer air-mass sensitivity fields were aggregated to contrast large-scale transport patterns between sites, and deposition rates were correlated with in situ $PM_{10}$ and with the CAMS European air quality reanalysis to evaluate the agreement between deposition and ambient concentration. Correlation analysis was also applied to examine relationships among particle classes.

https://doi.org/10.5194/egusphere-2026-5232
Preprint. Discussion started: 11 September 2026


In situ $PM_{10}$ observations were obtained from two regulatory air quality monitoring stations reporting under Directive 2008/50/EC, the Arnesano-Riesci station of the ARPA Puglia regional air quality monitoring network (RRQA), classified as a suburban background site and located approximately 2 km from the Lecce sampler, and the Gharb station on Gozo, operated by the Environment and Resources Authority (ERA) of Malta and classified as a rural background site, located $<$1.7 km from the San Lawrenz sampler. Both stations report $PM_{10}$ at daily resolution. Local meteorological data were obtained from the micrometeorological station of the Institute of Atmospheric Sciences and Climate of the National Research Council (CNR-ISAC) at Lecce, located approximately 1.5 km from the dry deposition sampler, and from the Gharb station at San Lawrenz.

Temporal variability in particle-type dominance was evaluated by linking marine (sea salt class) and mineral dust (clay minerals, (phyllo-)silicate/clay minerals, feldspars, other silicates and Ca-rich classes) classifications to sampling month, while size-resolved composition was analysed using kernel density-based particle-size distributions. Cumulative deposition behaviour was assessed by relating deposition rate (mg $m^{-2}$ $d^{-1}$) to deposition flux (mg $m^{-2}$) for the main particle groups.

The internal geochemical signature of the mineral dust fraction was characterized by computing the iron atomic proportion relative to the total detected elements for each particle. Finally, mixing state dynamics during peak dust episodes were evaluated by analysing the temporal evolution of silicate–sulfate and silicate–sea salt mixed particle fractions. Together, these analyses provide complementary context for the interpretation of the CWT results at the two Mediterranean receptor sites.

## 3 Results

The results are organized across four complementary scales of analysis. First, the size-resolved compositional structure of the deposited material is characterized, along with its geochemical coherence and variability between peak dust events and background conditions. Second, the temporal and seasonal dynamics of the dominant aerosol types are examined, including their mass flux and deposition intensity distributions. Third, the potential source regions associated with the deposited material are identified through trajectory-based analysis, from aggregated sensitivity fields down to class and size-specific patterns. Finally, local wind conditions at each receptor site are evaluated to assess the directional control on deposition at the immediate scale.

### 3.1 Particle-size–resolved composition

The compositional structure of the deposited material and its dependence on particle size were characterized through the relative contribution of each SEM-defined particle class, evaluated as a function of volume-equivalent diameter across the full study period (spring 2017 to winter 2018) at both receptor sites (Figure 4).

https://doi.org/10.5194/egusphere-2026-5232
Preprint. Discussion started: 11 September 2026


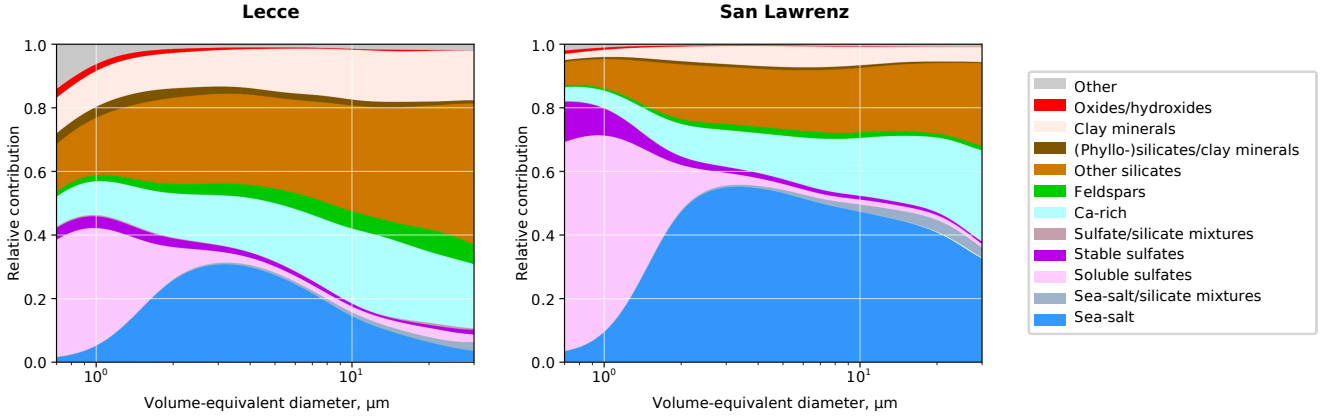


**Figure 4.** Size-resolved relative contribution of particle classes (2017–2018). Note that a kernel density estimator was used to regard all single particle size measurements, resulting in smooth curves.

Clear size-dependent variations in class contributions are observed at both sites. Major contributors like sea salt, other silicates, and soluble sulfates, reach relative contributions of approximately 30–60 % within specific diameter intervals, while minor classes such as oxides/hydroxides, feldspar, and sulfate–silicate mixtures remain generally below 5–10 % across most of the size spectrum. At Lecce, silicate-related classes constitute an important fraction over a broad diameter range, dominating particularly above 2 $\mu$m. Within this coarse-dominated regime, Ca-rich particles show a steady and increasing presence toward intermediate and coarse sizes. Sea salt is most prominent in the intermediate size range, while soluble sulfates contribute mainly within the submicron and lower micrometer fraction. At San Lawrenz, the size-resolved structure reveals a different compositional balance. Sea salt represents the dominant class across a wide range of diameters, peaking at nearly 60 % between approximately 1 and 15 $\mu$m, in contrast with the silicate-dominated structure observed at Lecce. Soluble sulfates at San Lawrenz account for over 70 % of the relative contribution at the submicron diameters before declining progressively toward larger sizes, a proportion notably higher than at Lecce.

The internal structure of these size-resolved distributions undergoes significant shifts depending on the deposition regime. To stratify sampling periods, intervals were classified as high-intensity dust intrusions (Top 5 peak events) or background conditions based on total particle deposition rate, where the dust signal was defined as the combined contribution of Ca-rich, feldspar, oxides/hydroxides, clay minerals and other silicates particles. As shown in Figure 5, during peak episodes, the mineralogical signature becomes dominant across the entire diameter spectrum at both sites, with silicate-related classes and Ca-rich particles collectively accounting for more than 80 % of the relative contribution. These mineral classes also constitute a persistent component during background conditions, though at a substantially lower proportion. Under these periods, the reduced dust signal allows the emergence of other sources, with marine aerosol influence and fine-fraction behavior becoming more evident. San Lawrenz, in particular, exhibits a higher prevalence of sea salt compared to Lecce, especially in the intermediate and coarse ranges (1–20 $\mu$m). Furthermore, both sites show a substantial recovery of the soluble sulfate contribution within the submicron fraction ($< 1$ $\mu$m) during background periods, a signal largely masked during high-intensity dust peaks.

https://doi.org/10.5194/egusphere-2026-5232
Preprint. Discussion started: 11 September 2026


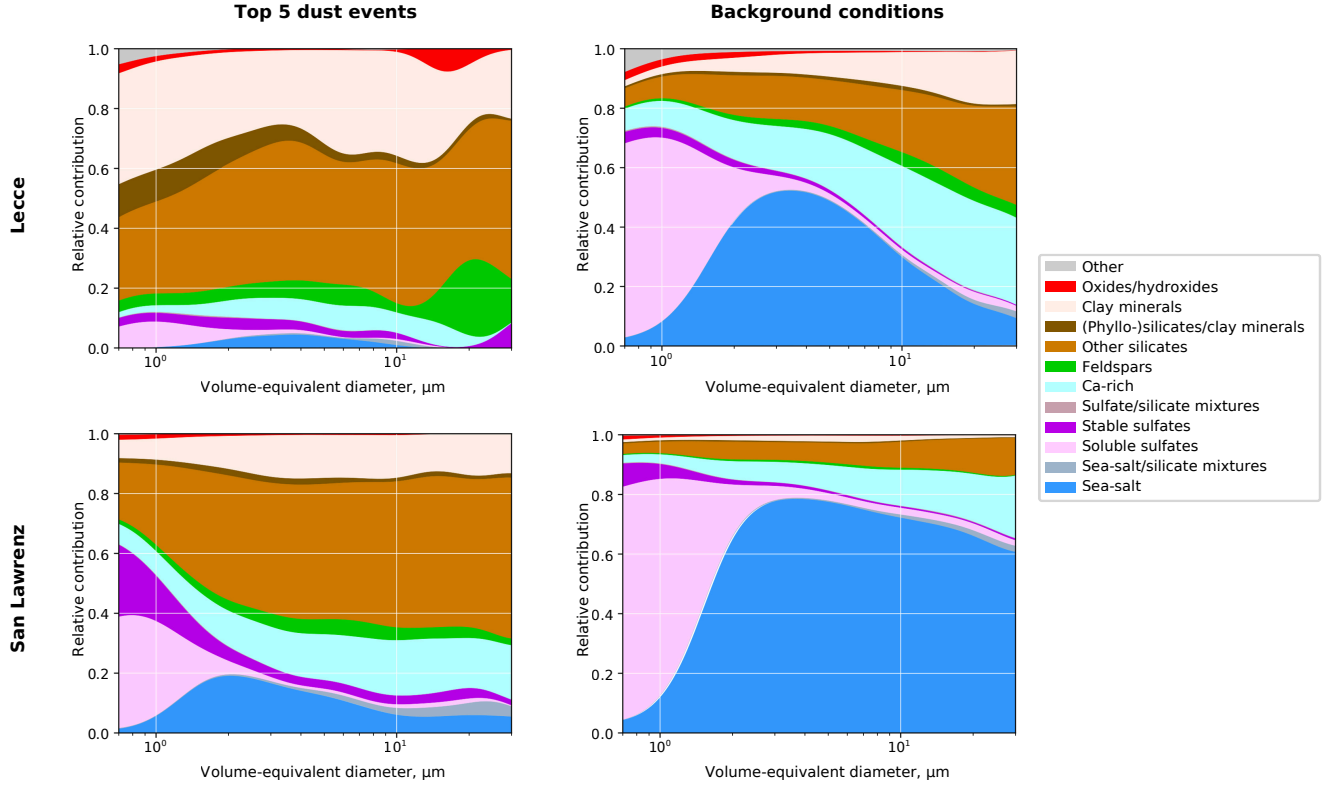


**Figure 5.** Size-resolved relative contribution of particle classes. The left columns show the integral of the 5 strongest dust particle number deposition events, where the right columns show background conditions, defined as the samples with the lowest dust number deposition rates whose cumulative contribution amounts to 20 % of the total dust number deposition at each site.

A further quantitative shift is identified in the internal balance of the mineral fraction, specifically in the proportion of Ca-rich particles relative to total mineral mass (silicates and Ca-rich classes combined). At Lecce, this proportion increases markedly from 3.6 % during peak events to 39 % under background conditions; a comparable trend is observed at San Lawrenz, where it rises from 18 % to 41 %. Although the absolute dust mass is lower during background periods, the mineral material present is characterized by a substantially higher relative abundance of calcium-rich components compared to the silicate-dominant peak episodes.

The geochemical coherence of these particle classes is further supported by Pearson correlation matrices of the number deposition rates of each class at both sites (Figure 6). A strong positive correlation ($r > 0.7$) is observed among other silicates, feldspars, clay minerals, and oxides/hydroxides, confirming their shared origin as a unified mineral dust complex. Notably, while these components are tightly coupled, the Ca-rich class shows a more moderate correlation with the primary silicates.

https://doi.org/10.5194/egusphere-2026-5232
Preprint. Discussion started: 11 September 2026


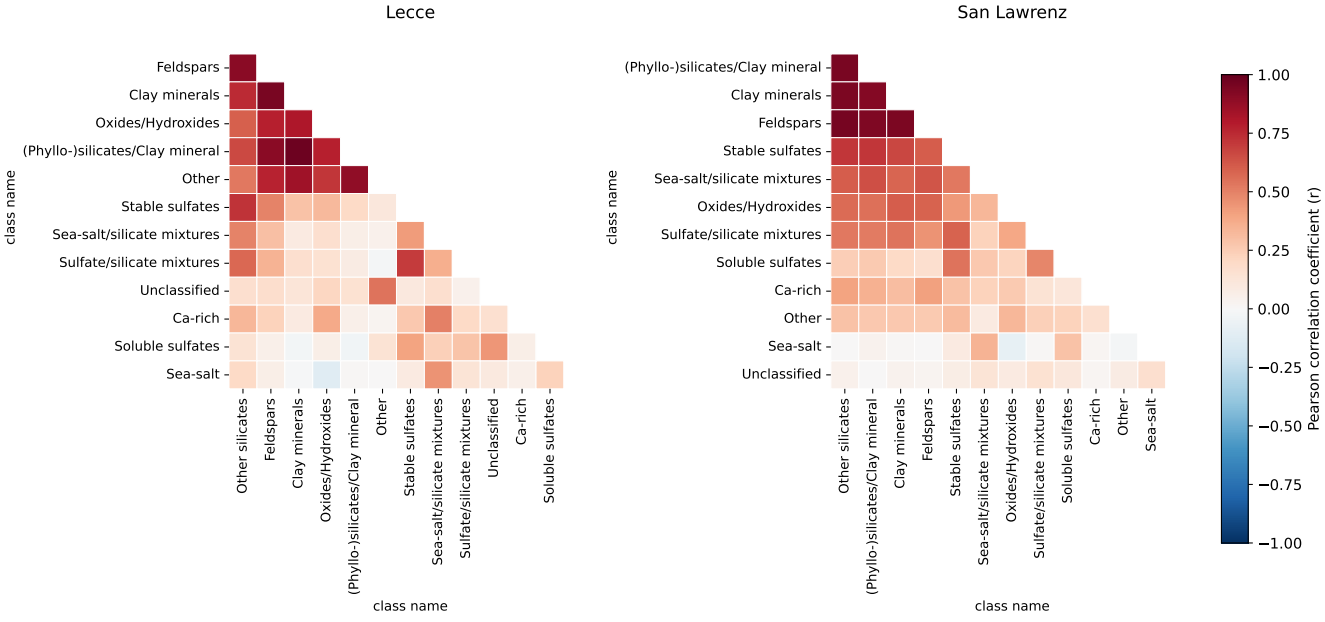


**Figure 6.** Pearson correlation matrices of major particle classes for the number deposition rates at Lecce and San Lawrenz.

## 3.2 Mineralogical enrichment diagnostics

To evaluate the mixing dynamics during peak dust deposition episodes, the temporal evolution of the major particle class mixing states was analyzed within five-sample windows centered on each peak event (Figure 7). In this analysis, mixtures were defined as the combination of silicates with sulfates (sulfate mix) and silicates with sea salt (sea-salt mix), and deposition rates were normalized to their maximum value within each event window to allow direct temporal comparison regardless of absolute mass load.

The results reveal that the mineral dust deposition peak does not mark the end of the event but rather could precede an upward trend in both the sulfate mix and sea-salt mix curves toward their own relative maxima. This phase lag, in which the peak relevance of the mixed fractions follows the dust peak, indicates that the termination of a Saharan intrusion is not an abrupt cessation but a gradual transition defined by progressive atmospheric processing.

https://doi.org/10.5194/egusphere-2026-5232
Preprint. Discussion started: 11 September 2026


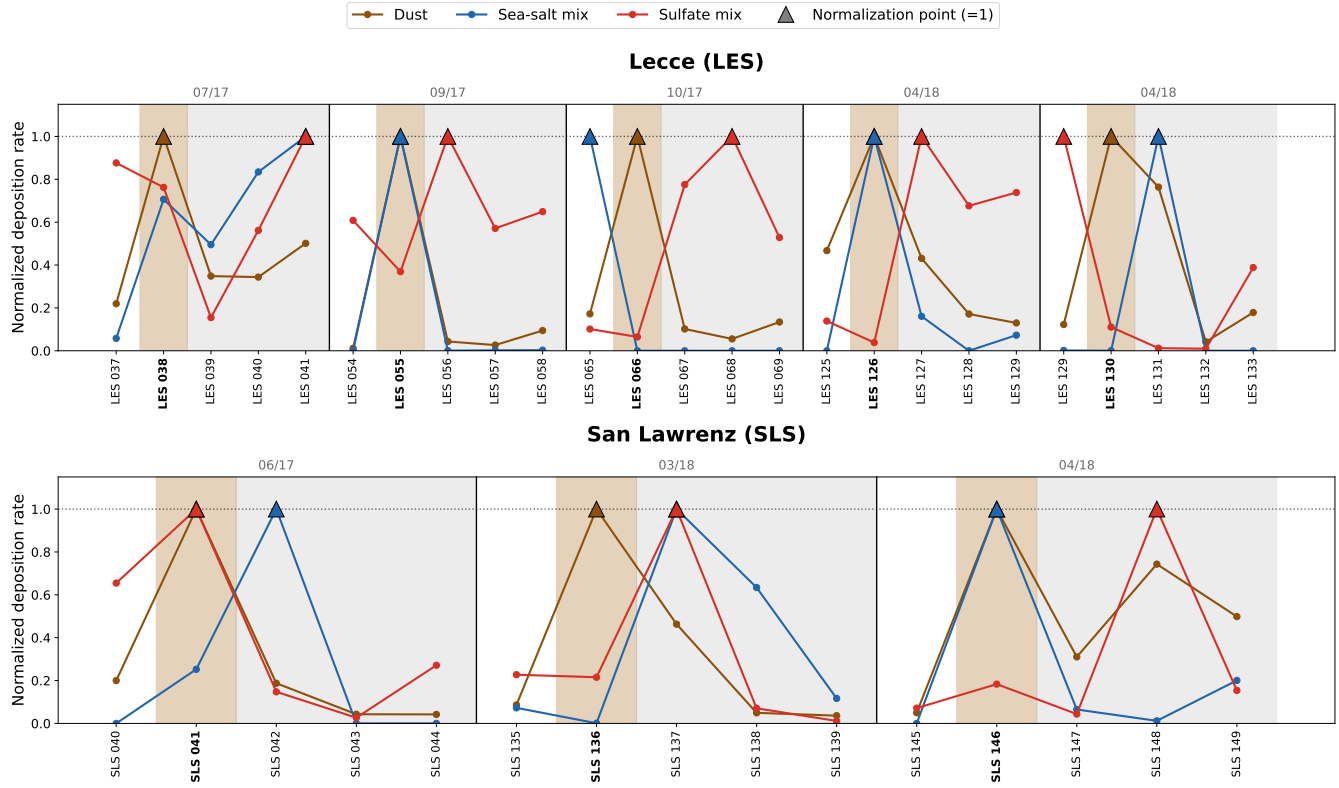


**Figure 7.** Temporal evolution of normalized deposition rates for mineral dust (brown), sea-salt mix (blue) and sulfate mix (red) during Saharan dust intrusion events at Lecce and San Lawrenz. Each event window comprises the sample preceding the dust deposition peak, the peak sample itself, and the three subsequent samples. Deposition rates are normalized to the maximum value reached by each particle class within its event window; the triangular marker on each curve indicates the sample at which that class reaches this maximum.

370 To complement this mixing dynamics analysis, the internal geochemical signature of the mineral dust fraction was further characterized using the iron atomic proportion relative to total detected elements, segmented into five particle size ranges and contrasted between peak and background conditions (Figure 8).

During peak deposition episodes, the iron proportion is consistently higher across all size fractions compared to background levels. Site-specific differences are also evident, Lecce exhibits higher Fe proportions than San Lawrenz during peak events, 375 while this relationship reverses under background conditions, where San Lawrenz exceeds Lecce. Across both sites, the finest fractions (diameters up to 2.5 $\mu$m) host the highest iron proportions, indicating a systematic enrichment of iron-bearing minerals in the fine-grained dust fraction.

https://doi.org/10.5194/egusphere-2026-5232
Preprint. Discussion started: 11 September 2026


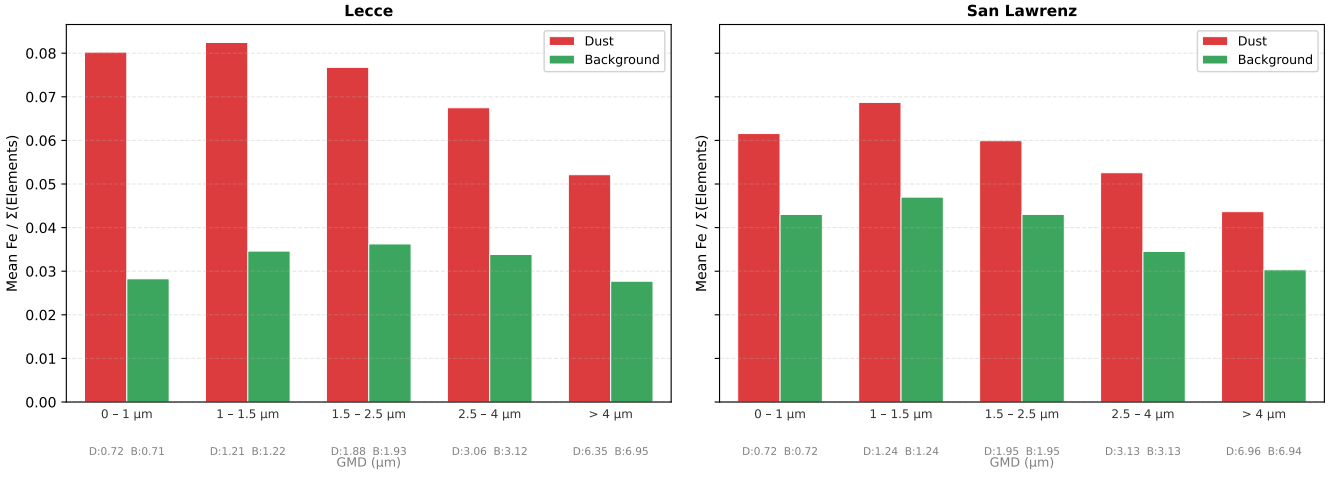


**Figure 8.** Iron contribution as a function of volume-equivalent diameter in mineral dust-classified particles during the five highest dust number deposition rate and background number deposition rate conditions at Lecce and San Lawrenz. The red bars show the mean iron atomic proportion for peak events, while the green bars for background.

### 3.3 Mineral dust and sea salt deposition: annual balance and seasonal variability

Over the 2017–2018 study period, mineral dust clearly dominates most samples at both sites, with each sample assigned to the component contributing the higher total deposited mass. At Lecce, mineral dust dominated 95 % of samples while sea salt dominated the remaining 5 %. At San Lawrenz, mineral dust dominated 69 % of samples and sea salt 31 %. When samples are instead classified by particle number, a different distribution appears. At Lecce, mineral dust dominated 74 % of samples and sea salt 26 %, while at San Lawrenz the distribution is nearly balanced, with 47 % mineral dust and 53 % sea salt. The share of samples dominated by mineral dust is consistently higher when classified by deposited mass than by particle number, whereas sea salt dominates a disproportionately larger share of samples by particle number, a contrast that is particularly pronounced at San Lawrenz.

Beyond this annual average perspective, the contrasting contributions of terrestrial and marine aerosols were further examined through the monthly proportion of mineral dust and sea salt-dominated events at both sites (Figure 9). For each month, the occurrence of each regime type was normalized by the total number of available samples in that month, allowing a direct comparison of relative dominance independent of sampling frequency.

https://doi.org/10.5194/egusphere-2026-5232
Preprint. Discussion started: 11 September 2026


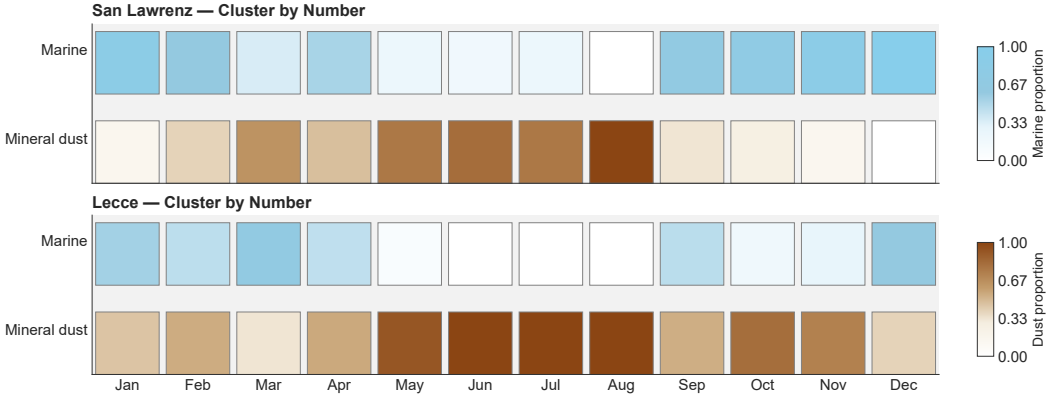


**Figure 9.** Monthly proportion of samples classified as marine- or mineral dust-dominated at San Lawrenz and Lecce, based on number deposition rate. For each month, the proportion is the number of samples assigned to a given regime divided by the total number of samples collected that month.

This monthly evaluation reveals marked seasonal shifts. Enhanced dust contributions are observed during late spring and summer at both sites, particularly from May through August, while sea salt fractions increase during winter and early spring. This seasonal modulation is more pronounced at San Lawrenz, where marine particles dominate winter counts, whereas at Lecce mineral dust remains the major contributor throughout most of the year despite seasonal fluctuations.

### 3.4 Size-resolved mass deposition trends

Complementing the proportional analysis described in the previous section, size-resolved mass deposition rates (dM/dlogd) were evaluated for mineral dust, sea salt, and sulfate at both receptor sites to examine their temporal and size-dependent variability (Figure 10).

https://doi.org/10.5194/egusphere-2026-5232
Preprint. Discussion started: 11 September 2026


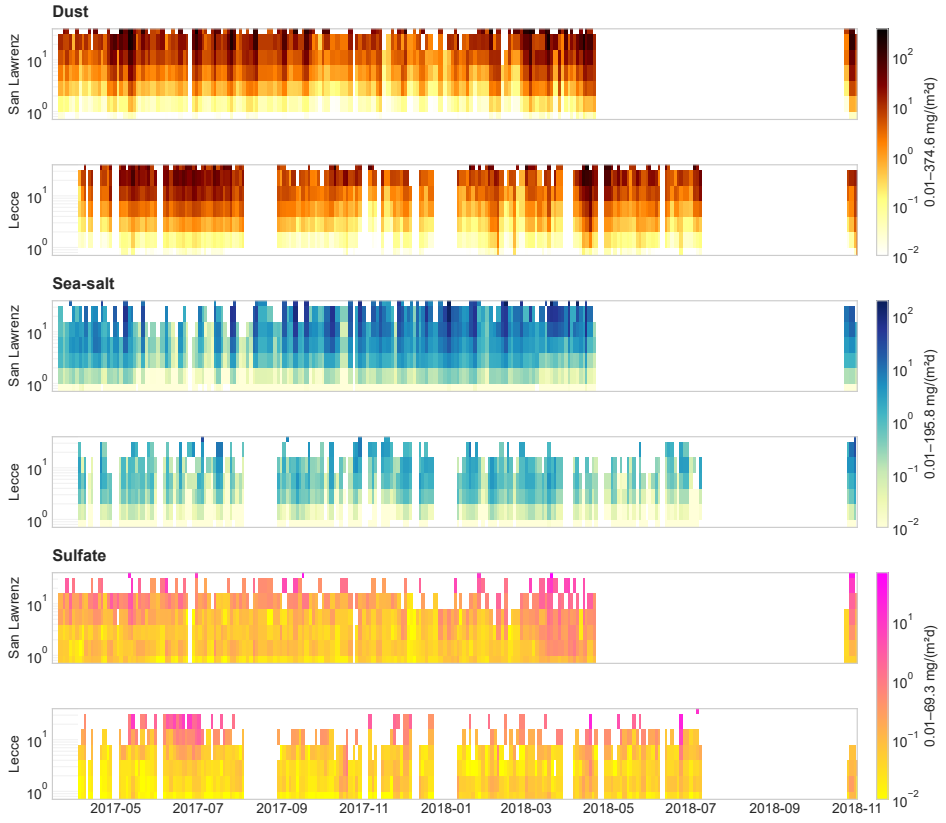


**Figure 10.** Size-resolved mass deposition rate (dM/dlogD) of mineral dust, sea salt, and sulfate particles as a function of particle volume-equivalent diameter ($\mu$m) and time, at San Lawrenz and Lecce.

Mineral dust deposition exhibits recurrent high-intensity episodes at both sites, predominantly within the intermediate and coarse size ranges above 2–3 $\mu$m, with maxima extending beyond 10 $\mu$m. Pronounced events are observed in May 2017 and during March–April 2018 at both sites, marked by enhanced coarse-mode contributions. Between major episodes, dust remains consistently detectable across most size classes, reflecting a sustained background presence.

By its part, sea salt deposition follows a broadly similar size regime, with dominant contributions in the intermediate and coarse fractions and comparatively lower intensities in the fine mode. The most pronounced sea salt episodes occur between January and April 2018 at San Lawrenz, characterized by intensified coarse-mode signals extending to larger diameters. Periods of markedly reduced sea salt deposition are observed during summer, particularly at Lecce. Coarse-mode deposition frequently reaches higher magnitudes at San Lawrenz, where elevated intensities are more evident at larger particle sizes.

Finally, sulfate deposition, although generally lower in magnitude than mineral dust and sea salt, also exhibits dominant contributions in the intermediate to coarse size range, with weaker but persistent signals in the fine fraction. The most pronounced sulfate episodes occur in April 2018 at San Lawrenz and in June–July 2018 at Lecce, characterized by enhanced deposition primarily in the intermediate particle size range rather than in the largest coarse bins.

https://doi.org/10.5194/egusphere-2026-5232
Preprint. Discussion started: 11 September 2026


### 3.5 Deposition intensity contribution and cumulative flux

Since deposition rates span a wide range of intensities, their relative contribution to the total accumulated mass is not uniform. To quantify how the integrated flux builds up across increasing deposition rates, cumulative deposition curves were constructed for each grouped particle class, complemented by a cumulative duration analysis.

In terms of mass (Figure 11b), mineral dust is the primary driver of the depositional budget at both sites. The dust curves lie furthest to the right on the intensity axis and rise steeply across the high-intensity range (10 to 300 mg $m^{-2}$ $d^{-1}$). At San Lawrenz, dust reaches the highest overall intensities and a total integrated flux of $1.11 \times 10^4$ mg $m^{-2}$, nearly double that at Lecce ($6.19 \times 10^3$ mg $m^{-2}$). Sea salt occupies an intermediate position but differs notably between sites. At San Lawrenz the sea-salt curve is shifted toward higher deposition rates, with prominent step-like increments reflecting discrete high-energy maritime pulses, and reaches a total flux of $6.32 \times 10^3$ mg $m^{-2}$. At Lecce the curve is shifted markedly toward lower intensities, with a much more attenuated contribution of $4.40 \times 10^2$ mg $m^{-2}$, indicating that the marine influence at this site occurs at lower intensities. Sulfate contributes the smallest flux at both sites ($1.62 \times 10^2$ mg $m^{-2}$ at Lecce and $3.89 \times 10^2$ mg $m^{-2}$ at San Lawrenz), and its cumulative curves lie furthest to the left, following a two-phase structure with a long interval of negligible growth at low intensities followed by a sharp, near-vertical rise in the upper tail.

The three classes are episodic, but to different degrees. The five highest-rate events account for approximately 20 % of the total dust mass, 25 % of the sea-salt flux, and 40 % of the sulfate mass, in each case at both sites. Sulfate is therefore the most concentrated in time, consistent with the two-phase shape of its cumulative curves; dust, whose curve rises more gradually across the moderate-to-high intensity range, is the least concentrated, although a fifth of its mass still arrives in five sampling events. These events are shown individually in Figure 11c together with their central 95 % intervals. The intervals overlap substantially between events within a given class and site, so the ranking of individual episodes should not be interpreted as a strict ordering. The 95 % confidence intervals for all samples collected during the study period are presented in supplementary Fig. S3.

In terms of sampling time (Figure 11a), mineral dust shows a synchronized pattern at both sites, with intensities above 50 mg $m^{-2}$ $d^{-1}$ occurring approximately 15 % of the time. A similar fraction of the time falls below 3 mg $m^{-2}$ $d^{-1}$, suggesting that although dust displays considerable variability, both the lowest and the highest intensities are less frequent than moderate ones. San Lawrenz records a more extensive set of low-intensity events than Lecce. Sulfate occupies the lower end of the intensity spectrum, with both sites recording predominantly low background levels ($< 1$ mg $m^{-2}$ $d^{-1}$), which makes high-intensity sulfate events rare. Sea salt again shows the biggest contrast between sites; at San Lawrenz, high-intensity marine pulses occur frequently enough to overlap the mineral dust range, whereas at Lecce this frequency collapses toward low-intensity regimes.

Read jointly, the two cumulative distributions show that a small fraction of the sampling time accounts for a large fraction of the deposited mass. At Lecce, half of the total dust mass was deposited at rates exceeding approximately 30 mg $m^{-2}$ $d^{-1}$, which were sampled during about 13 % of the total sampling time; at San Lawrenz, the corresponding rate was approximately 80 mg $m^{-2}$ $d^{-1}$, sampled during about 10 % of the time.

https://doi.org/10.5194/egusphere-2026-5232
Preprint. Discussion started: 11 September 2026


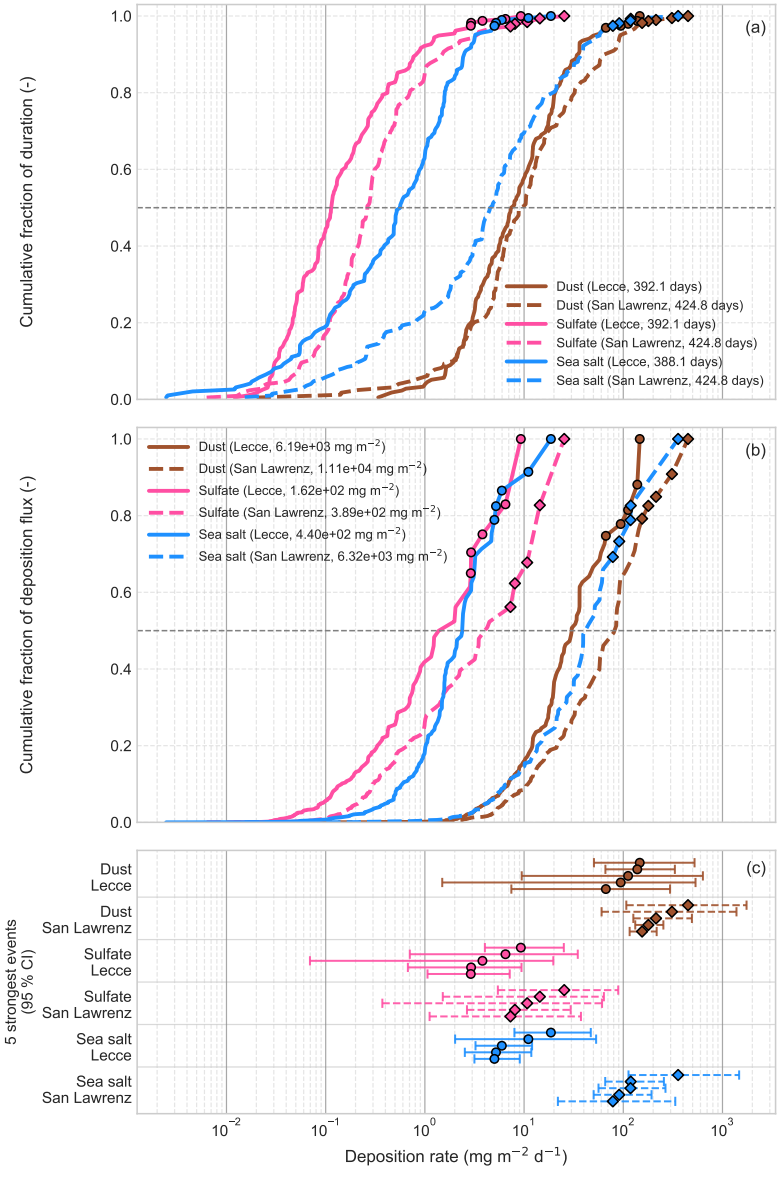


**Figure 11.** Cumulative distributions of deposition rate for mineral dust, sulfate and sea salt at Lecce and San Lawrenz. Sampling events were ranked by deposition rate (mg m$^{-2}$ d$^{-1}$) and their durations (a) or deposited masses (b) cumulatively summed and normalized to the corresponding total, given in the legends. Symbols mark the five events with the highest deposition rate for each particle class and site, shown separately in (c) with the central 95 % interval, which reflects the uncertainty and heterogeneity of deposition.

### 3.6 Comparison of boundary-layer sensitivity fields

Given the differences in cumulative deposition structure between Lecce and San Lawrenz described in the previous section, the dominant transport sensitivity patterns were examined to assess whether these contrasts are also reflected at the regional

https://doi.org/10.5194/egusphere-2026-5232
Preprint. Discussion started: 11 September 2026


scale. The independently log-transformed and normalized accumulated boundary-layer sensitivity fields were subtracted (Lecce minus San Lawrenz), where positive values indicate grid cells contributing proportionally more to the normalized accumulated sensitivity of Lecce, and negative values indicate relatively stronger contributions to San Lawrenz (Figure 12).

Positive differences are primarily observed over parts of eastern and northeastern Europe, including areas north of the Black Sea and sections of the Balkan Peninsula, indicating a proportionally stronger transport sensitivity of Lecce toward these regions. In contrast, negative differences are concentrated over North Africa and portions of the eastern Mediterranean, extending into the Levant region, reflecting the comparatively stronger sensitivity of San Lawrenz to these source areas. Across the western Mediterranean and the Iberian Peninsula, sensitivity contrasts remain comparatively weak.

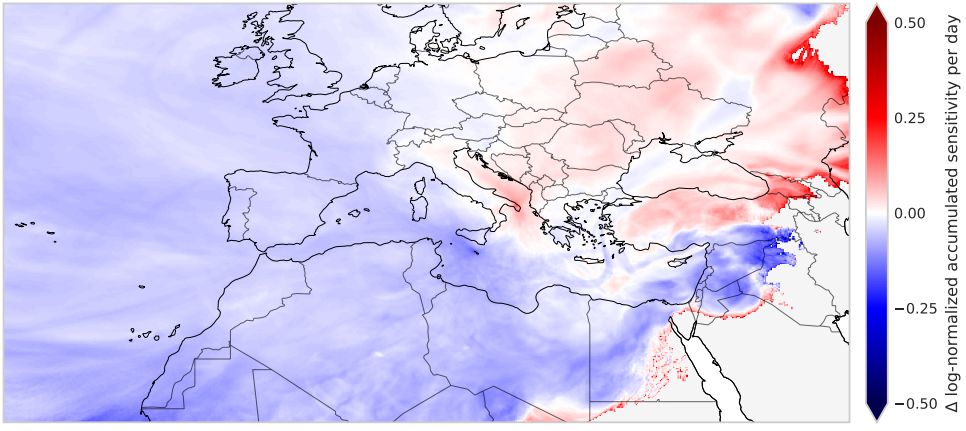


**Figure 12.** Comparison of the air sheds contributing to atmospheric transport at Lecce and San Lawrenz. Values show the relative difference in normalized transport sensitivity between the two sites, with red indicating greater sensitivity at Lecce and blue at San Lawrenz.

### 3.7 DCWT ($PM_{10}$ proxy)

The spatial contrasts identified in the accumulated sensitivity fields were further examined at the scale of individual sampling periods for each site. Accordingly, DCWT fields were computed for each interval using hourly $PM_{10}$ concentrations as the concentration term and boundary-layer-integrated FLEXPART sensitivity fields as transport weighting.

To illustrate the spatial structure associated with peak deposition conditions, representative examples are shown for the five intervals exhibiting the highest total dust deposition rates at each site (Figure 13). At Lecce, enhanced DCWT values extend broadly across the central and eastern Mediterranean, including southeastern Europe and, in some cases, long-range corridors from the North Atlantic. In contrast, at San Lawrenz the pattern is different, the highest values are consistently concentrated over northern Africa, particularly Libya, Tunisia, and Algeria, and the adjacent central Mediterranean, reflecting a more spatially confined and compact configuration.

These representative cases highlight distinct and recurrent spatial configurations associated with elevated deposition conditions at the two sites, providing the physical basis for the MA-CWT fields presented in the following section.

https://doi.org/10.5194/egusphere-2026-5232
Preprint. Discussion started: 11 September 2026


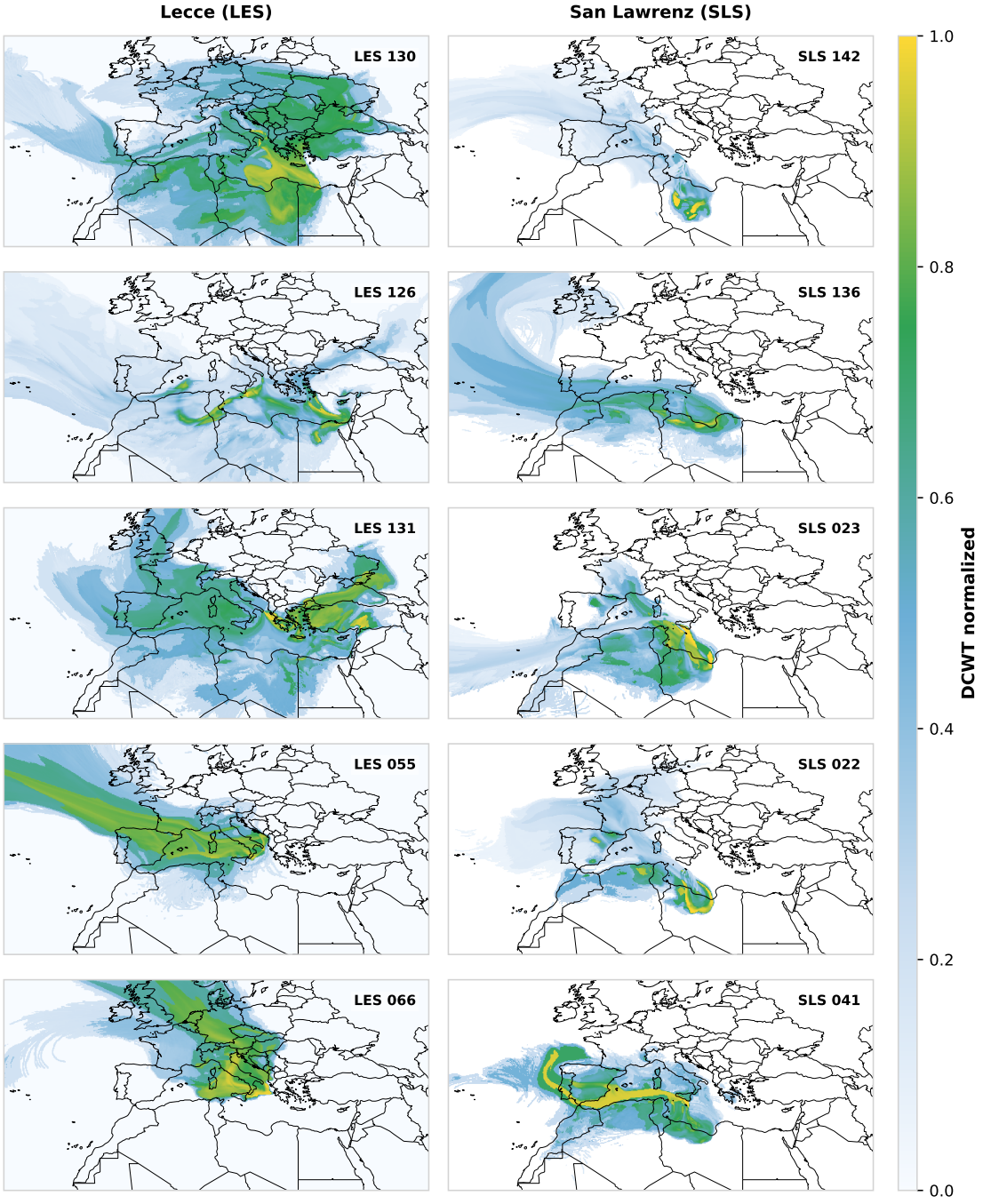


**Figure 13.** Direct Concentration-Weighted Trajectory (DCWT) fields for the five sampling intervals with the highest total (mass-based) dust deposition rate at Lecce and San Lawrenz. Each panel shows the probable source regions and transport pathways of the air masses associated with elevated $PM_{10}$ concentrations during that specific sampling interval.

https://doi.org/10.5194/egusphere-2026-5232
Preprint. Discussion started: 11 September 2026


### 3.8 General classes deposition-based trends (MA-CWT)

While the DCWT reflects source regions associated with elevated atmospheric $PM_{10}$ concentrations, it does not explicitly distinguish the material that ultimately reached the surface. A MA-CWT analysis was therefore performed, replacing the concentration term with class-specific dry-deposition rates derived from SEM analysis, while the normalized DCWT fields provided the transport weighting for each sample. The resulting maps represent potential source regions specifically associated with deposited material of each particle class (Figure 14).

Pronounced class-dependent and inter-site contrasts emerge in the spatial distribution of source regions. For clay minerals, Lecce exhibits a comparatively broad regional footprint, with maxima over the northwestern Saharan region and the southern Mediterranean basin. These signals extend further across the Iberian Peninsula and into southeastern Europe, a spatial reach notably absent in the more confined San Lawrenz fields, where dominant contributions are concentrated over northern Africa, particularly central Algeria, with only limited extension into European sectors.

Sea salt exhibits distinct spatial source configurations between the two receptor sites. At both locations, signals over the Mediterranean Sea reflect the importance of nearby marine sectors. However, differences arise in the Atlantic contribution. In Lecce, the pattern extends farther into the northeastern Atlantic domain, indicating a comparatively stronger influence from higher-latitude Atlantic transport pathways. In contrast, San Lawrenz is more clearly centered over the western and central Mediterranean, with Atlantic influence restricted to regions west of the Iberian Peninsula and along the eastern Atlantic margin near Portugal. These divergent transport patterns are accompanied by a striking disparity in the total deposited mass. The total sea-salt flux at San Lawrenz reaches 6.3 x $10^3$ mg/$m^2$, representing an order of magnitude increase over the 4.4 x $10^2$ mg/$m^2$ recorded at Lecce.

For secondary and mixed components, the inter-site contrast shifts geographically. Soluble sulfates in Lecce are characterized by maxima over central and southeastern Europe, including the Balkan region, whereas at San Lawrenz enhanced values are displaced toward the Iberian Peninsula and northern Africa, accompanied by broader Atlantic influence. A comparable redistribution is observed for oxides and hydroxides, with Lecce emphasizing northern African regions and western Asia and San Lawrenz showing stronger extension into western and central Europe.

https://doi.org/10.5194/egusphere-2026-5232
Preprint. Discussion started: 11 September 2026


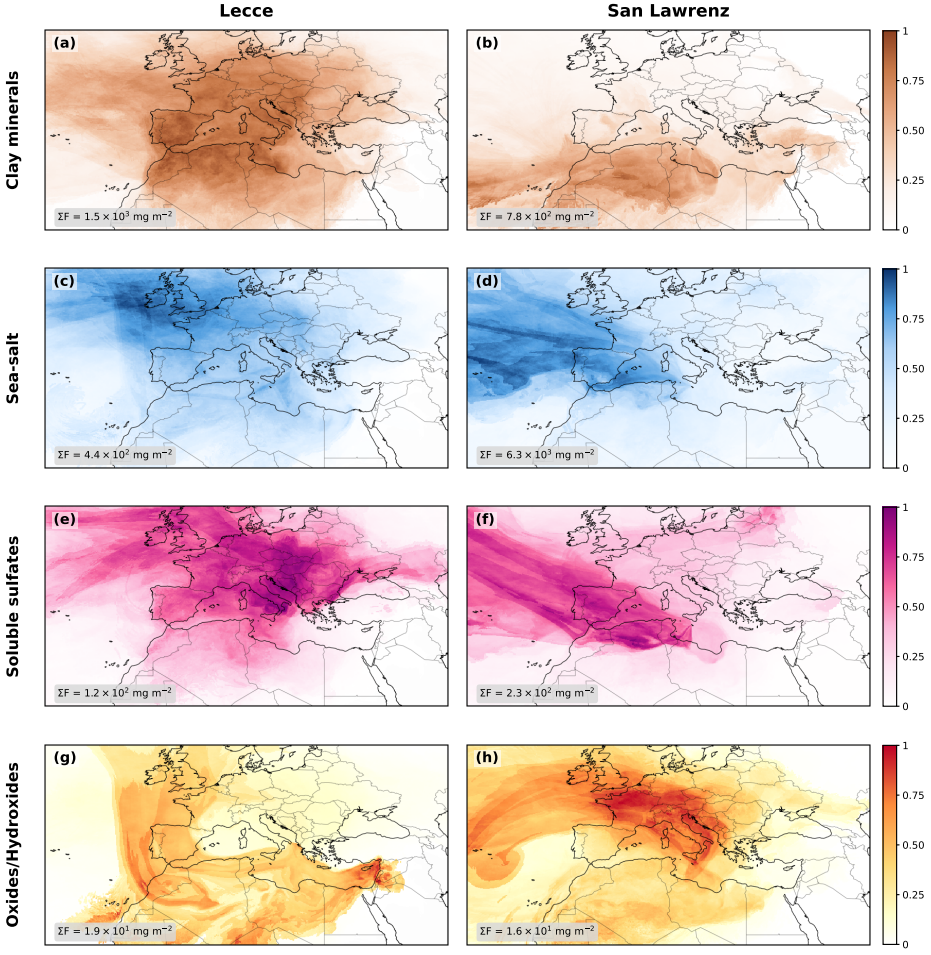


**Figure 14.** Model-Assisted Concentration-Weighted Trajectory (MA-CWT) fields for clay minerals, sea-salt, soluble sulfates and oxides/hydroxides at Lecce and San Lawrenz. Each panel shows the probable source regions and transport pathways of the air masses associated with the deposited mass of each particle class.

The size-resolved breakdown of these classes, detailed in supplementary Figs. S4 and S5, clarifies the spatial organization of the aggregated fields. For clay minerals, Lecce exhibits a broad size-dependent pattern, with the fine fraction linked primarily to northwestern Africa, the coarse fraction concentrated over northern African regions, and the supercoarse fraction extending toward European land areas including northern Europe. At San Lawrenz, in contrast, the pattern remains largely confined to northern Africa across all fractions, though its spatial extent narrows as particle size increases.

Sea salt displays a distinct transition, where in Lecce, the fine fraction reflects nearby Mediterranean marine sources, but shifts toward the North Atlantic as particle size increases, becoming dominant in the supercoarse fraction. Conversely, in San Lawrenz, all sea salt fractions remain centered over the western Mediterranean near the southern coasts of Spain and France, with only the supercoarse fraction showing a clear contribution from Atlantic sectors west of the Iberian Peninsula.

https://doi.org/10.5194/egusphere-2026-5232
Preprint. Discussion started: 11 September 2026


Secondary and mixed components exhibit further regional contrasts. Soluble sulfates in Lecce are associated primarily with nearby European regions, with increasing influence from the Balkans in the coarse and supercoarse fraction, while in San Lawrenz, the Iberian Peninsula dominates the fine and coarse fractions, and the supercoarse fraction shifts toward northern Africa, particularly Algeria. Finally, for oxides and hydroxides, local European sources around northern Italy dominate the fine and coarse fractions in Lecce, with the supercoarse fraction linked to northern Africa, whereas in San Lawrenz, the supercoarse fraction is associated with central and northern Europe, while the fine and coarse fractions are dominated by northern Africa and European regions.

### 3.9 Specific groups deposition-based trends (MA-CWT)

Building on the class-specific patterns described in the previous section, two particle groups of particular interest were analyzed separately: Pb-containing particles and aggregated mineral dust (Figure 15).

For Pb-containing particles (Figure 15a–b), spatial contrasts between the two sites are noticeable. At Lecce, enhanced MA-CWT values are distributed across the western and central Mediterranean, including the Iberian Peninsula, southern France, and Italy, with extensions into central Europe. At San Lawrenz, maxima are concentrated over North Africa, particularly the western Sahara and Morocco, with an extension into Algeria and Tunisia, regions that would not be expected to be the main contributors to the observed Pb-containing particles. This distribution is more likely to reflect a limitation of the approach, since the weighting is applied along the modelled transport pathways and contributions from local or near-field sources are not resolved.

For aggregated mineral dust (Figure 15c–d), both sites exhibit dominant signals over North Africa and the central Mediterranean basin. At Lecce, peak values extend across northern Algeria, Tunisia, and into the western Mediterranean, with additional influence toward southern Europe. At San Lawrenz, the strongest contributions are centered over northern Africa, particularly Libya and adjacent Saharan regions, with a comparatively reduced extension into Europe.

https://doi.org/10.5194/egusphere-2026-5232
Preprint. Discussion started: 11 September 2026


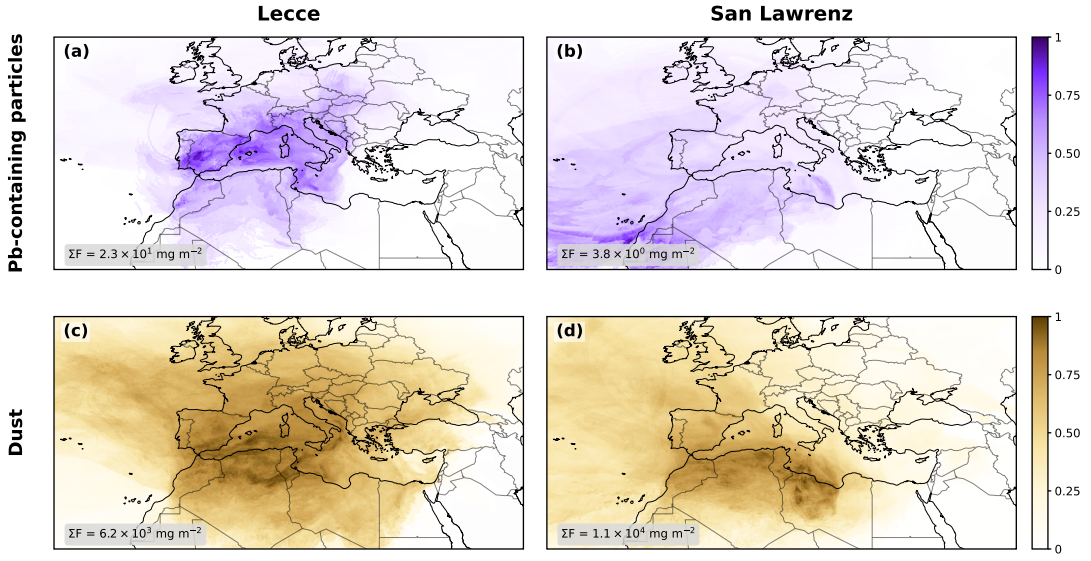


**Figure 15.** Model-Assisted Concentration-Weighted Trajectory (MA-CWT) fields for Pb-containing particles and dust at Lecce and San Lawrenz. Each panel shows the probable source regions and transport pathways of the air masses associated with the deposited mass of each particle class.

The temporal modulation of the dust patterns was further assessed by aggregating the DCWT fields seasonally, separating boreal summer (April to September) from boreal winter (October to March). At both sites, summer potential sources originate from Algeria, Tunisia and Libya and show the longest transport range across the Mediterranean. During winter, signals become more localized, Lecce shifts toward regional sources in the central Mediterranean and Italy, while San Lawrenz transport distances shorten, concentrating just near Libya. As seen in Figure 16, San Lawrenz presents a clearer deposition signal than Lecce across both seasons, though both sites follow a synchronized seasonal pattern of broad regional transport in summer and more restricted proximal sources in winter.

Beyond these transport pathways, a contrast emerges in the magnitude of the dust flux between sites. San Lawrenz records a higher total dust deposition rate than Lecce across both seasons, a difference that becomes particularly pronounced during winter. This variation is primarily driven by the internal balance of the mineral fraction, specifically the Ca-rich particle class. During winter, while Lecce records a minimal Ca-rich deposition of only 2.5 x $10^2$ mg/m$^2$, San Lawrenz reaches 3.1 x $10^3$ mg/m$^2$. A similar though less extreme trend is observed in summer, with San Lawrenz maintaining a high Ca-rich load of 3.1 x $10^3$ mg/m$^2$ compared to 1.1 x $10^3$ mg/m$^2$ at Lecce.

This inter-site contrast between the two sites resides in the super-coarse mode. At both sites the deposited Ca-rich mass is dominated by particles larger than 10 $\mu$m (87.2 % at Lecce, 94.9 % at San Lawrenz), which represent only 3.9 % and 8.0 % of the deposited particle number. The mass flux of this class is therefore determined by few large particles, while the numerous fine particles remain negligible for the deposited mass.

https://doi.org/10.5194/egusphere-2026-5232
Preprint. Discussion started: 11 September 2026


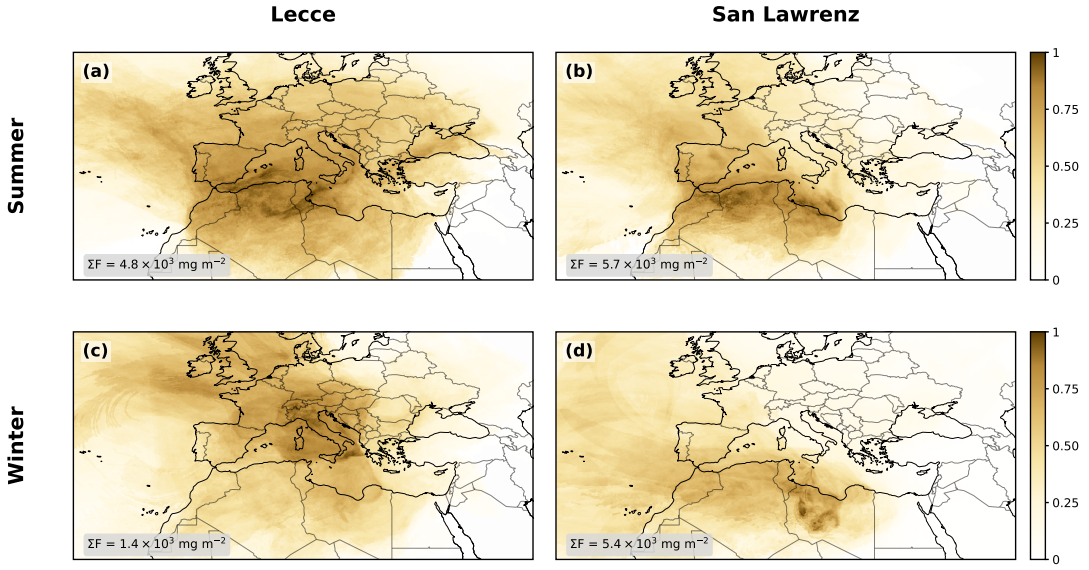


**Figure 16.** Model-Assisted Concentration-Weighted Trajectory (MA-CWT) seasonal fields for dust at Lecce and San Lawrenz. Each panel shows the probable source regions and transport pathways of the air masses associated with the deposited mass of each particle class for each season.

### 3.10 Local wind influence: pollution roses

Complementing the regional-scale source analysis presented in the previous sections, local wind conditions were evaluated to assess immediate transport and deposition dynamics at each receptor site. Pollution roses were constructed for mineral dust and sea salt, segmented by three particle diameter ranges: fine ($< 2.5$ $\mu$m), intermediate (2.5–10 $\mu$m), and coarse ($> 10$ $\mu$m). In the polar representation, angle denotes wind direction, radial distance corresponds to wind speed, and color intensity reflects the normalized magnitude of deposition within each direction-velocity bin (Figure 17).

At Lecce, dust deposition is predominantly associated with NNE winds, with a secondary SSE signal that scales with particle size. For the fine fraction, peak deposition occurs at moderate wind speeds (2.5–5 m/s), while for the coarse fraction deposition rates increase with wind speeds exceeding 5 m/s, particularly within the SSE sector. Sea salt deposition exhibits a clear size-dependent directional shift. The fine fraction peaks under southerly winds with a widespread directional distribution, whereas the intermediate fraction shows a dual maximum toward the northwest and south sectors. Finally, the coarsest particles are predominantly associated with moderate north-northwesterly winds.

Regarding San Lawrenz, the directional structure of both, dust and sea salt deposition, exhibits distinct size-dependent patterns. Coarse dust deposition is primarily associated with southerly winds at low to moderate wind speeds ($< 6$ m/s). In contrast, the fine and intermediate fractions show a more diffuse multi-directional pattern, with a dominant enhancement from the east-northeast at higher wind speeds reaching up to 15 m/s. Sea salt deposition shows a consistent western to west-northwesterly orientation across all size fractions. However, while the total mass deposition for the coarse fraction is concentrated in the NW

https://doi.org/10.5194/egusphere-2026-5232
Preprint. Discussion started: 11 September 2026


sector at moderate speeds (6–12 m/s), the fine fraction retains this western dominance while exhibiting a broader directional spread toward the east-northeast.

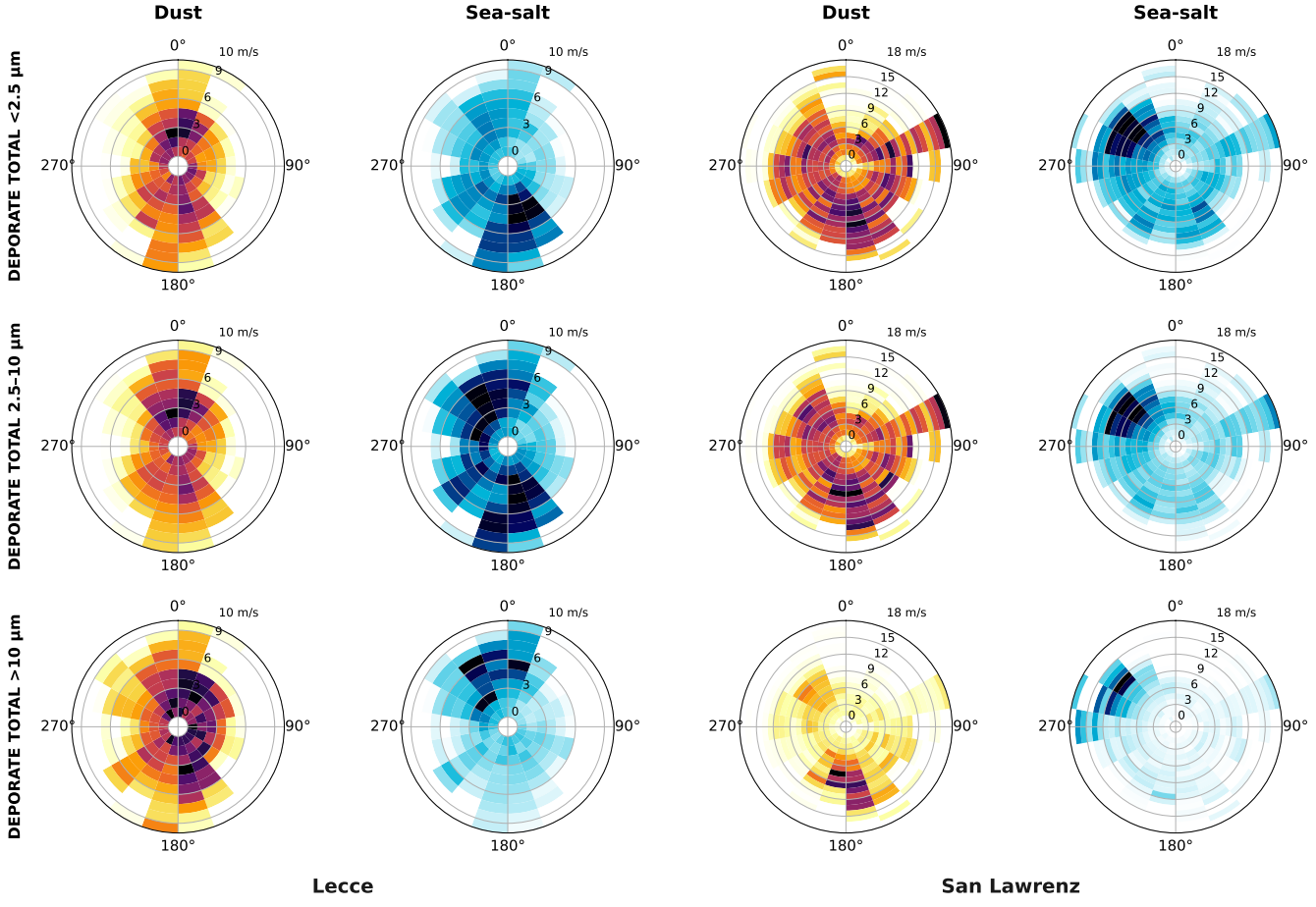


**Figure 17.** Size-resolved normalized pollution roses for mineral dust and sea salt at Lecce and San Lawrenz. In each polar plot, color intensity represents the normalized deposition magnitude within each direction–speed bin.

### 3.11 Correlation Analysis between Particle Deposition Rates and Atmospheric $PM_{10}$ Concentrations

Having established the spatial and dynamical structure of deposition sources across scales, the consistency between particle deposition rates and atmospheric $PM_{10}$ concentrations was evaluated to assess the coherence of the measurement framework.

For the total deposition rate, correlations are low to moderate at both sites. At Lecce, values reach r = 0.46 with CAMS and r = 0.25 with in situ measurements at Arnesano-Riesci, while at San Lawrenz correlations yield r = 0.36 with CAMS and r = 0.43 with Gharb measurements. Two factors are expected to weaken these associations. First, the deposition stations and the air quality monitoring sites are separated by approximately 2 km at Lecce and <1.7 km at San Lawrenz, which introduces local variability. Second, and more fundamentally, the total deposition rate includes the supercoarse and giant fractions, which

https://doi.org/10.5194/egusphere-2026-5232
Preprint. Discussion started: 11 September 2026


lie beyond the transmission range of a $PM_{10}$ inlet. This interpretation is supported by the increase in correlation when the analysis is restricted to the fine deposited fraction ($< 10$ $\mu$m). This threshold is not strictly equivalent to the $PM_{10}$ cut, since the deposition data are resolved by volume-equivalent diameter whereas $PM_{10}$ is defined in aerodynamic terms, but it isolates the size range in which both datasets overlap. At Lecce, correlations increase to r = 0.74 with CAMS and r = 0.51 with Arnesano-Riesci, while at San Lawrenz they reach r = 0.66 with CAMS and r = 0.78 with Gharb.

Furthermore, the reliability of the CAMS European air quality reanalysis is supported by its strong agreement with local air quality measurements, yielding coefficients of r = 0.72 at Lecce and r = 0.84 at San Lawrenz, thereby validating its use as a robust reference for evaluating particulate dynamics at both study sites.

## 4 Discussion

### 4.1 Contrasting aerosol regimes at Lecce and San Lawrenz

The silicate-dominated composition at Lecce and the sea-salt-dominated composition at San Lawrenz arise from different combinations of physical geography and large-scale circulation. The first factor is the distance to the coast. San Lawrenz, $<$ 900 m from the shoreline, lies within the emission zone of fresh marine aerosol, where wave breaking maintains a sea salt flux over a wide size range (Bruch et al., 2021; Deike, 2022; Deike et al., 2022; Rizzo et al., 2020). Lecce receives a comparable coastal air mass (Cesari et al., 2018; Contini et al., 2010), but its position 10 km inland is expected to remove the largest particles through size-selective gravitational settling before they reach the receptor, as reported for marine aerosol transported inland (Tedeschi and Piazzola, 2011) and in line with the size fractionation described across other offshore transport gradients (Flores et al., 2021; Kost and Stoll, 2023; Ma et al., 2022). Accordingly, the marine mass contribution at Lecce falls to 5 % of the annual deposited mass, an order of magnitude below San Lawrenz ($4.40 \times 10^2$ mg m$^{-2}$ against $6.32 \times 10^3$ mg m$^{-2}$).

Large-scale circulation acts as a second, independent control. At San Lawrenz, in the western basin, the composition alternates seasonally between summer Saharan dust intrusions, intensified by the Saharan Air Layer (Chiapello et al., 2021; Tsamalis et al., 2013; Varga et al., 2014), and marine-dominated conditions driven by the stronger winds and higher wave activity of the winter Mediterranean circulation (Dayan, 2011; Kishcha et al., 2011; Koçak et al., 2007; Liora et al., 2015; Pay et al., 2012). Over southern Italy, where Lecce is located, Saharan intrusions are superimposed on a persistent continental background transported from central, eastern and north-eastern Europe, a recurrent source of sulfate, black carbon and anthropogenic trace metals reported by long-term measurements at Lecce and the surrounding region (Caggiano et al., 2011; Di Gilio et al., 2015; Perrone et al., 2012; Petroselli et al., 2018; Sprovieri et al., 2011).

This continental overprint maintains the silicate-dominated signature at Lecce throughout the year, including periods of weak Saharan activity (Figure 9). The back-trajectory analysis supports this separation; Lecce is more frequently linked to north-eastern European air masses, and San Lawrenz to North African sources (Figure 12). The combination of air-mass origin and distance to the coast produces a compositional difference between the two sites that extends across particle classes, sizes and seasons.

https://doi.org/10.5194/egusphere-2026-5232
Preprint. Discussion started: 11 September 2026


### 4.2 Aerosol aging, mixing, and potential biogeochemical impacts

In several of the high deposition episodes, the mixed particle fractions follow the mineral dust pulse. Both silicate-sulfate and silicate-sea-salt mixtures reach their highest proportions during the dissipation phase, after the dust peak (Figure 7).

This phase lag indicates that the atmospheric processing of mineral particles intensifies as the intrusion weakens, in agreement with the known aging behaviour of mineral dust. On initial arrival, the aerosol population is dominated by freshly emitted mineral particles whose composition reflects the crustal source material, mainly $SiO_2$, $Al_2O_3$, $Fe_2O_3$, MgO and CaO, with limited surface modification (Dall'Osto et al., 2020; Goudie and Middleton, 2001). As the plume disperses and the particle concentration declines, the remaining mineral particles accumulate longer atmospheric residence times and greater exposure to reactive gases, and heterogeneous reactions on their surfaces become more efficient (Dall'Osto et al., 2010; Li et al., 2012; Liu et al., 2018; Sullivan et al., 2007). Sulfate uptake intensifies through $SO_2$ oxidation on $Al_2O_3$, CaO and $Fe_2O_3$, contributing 20–30 % of total sulfate during dust episodes (Chen et al., 2023; Liang et al., 2022; Tian et al., 2021; Yang et al., 2024), while acid displacement by $SO_2$ provides a further pathway for surface modification, especially on $CaCO_3$ and in more complex mixtures (Tian et al., 2021; Yang et al., 2020; Zhou et al., 2021). Particles with longer residence times are also more likely to interact with marine aerosol, increasing the probability of internal mixing between mineral dust and sea salt within the marine atmospheric boundary layer (MABL). In this environment, relative humidity above 80 % favours hygroscopic growth and physical adhesion, producing hybrid dust-salt particles that can be identified, for example, from lidar depolarization signatures (Becagli, 2022; Shrestha et al., 2026).

However, atmospheric aging is not observed in all cases. Transatlantic studies document dust that remains unprocessed after long-range transport (Aryasree et al., 2024). Nonetheless, the statistically detectable aging signal during the dissipation phase of the episodes analysed here indicates that Mediterranean conditions were sufficiently favourable for heterogeneous processing to leave a quantifiable imprint. The aerosol deposited during the dissipation phase is therefore chemically transformed, with possible consequences beyond the atmospheric column. Freshly emitted mineral iron is held predominantly in insoluble crystalline phases, with solubilities below 0.5 % near source regions (Li et al., 2020; Rodríguez et al., 2021; Shi et al., 2012), and acid processing during transport raises this fraction to 1–12 % (Perron et al., 2020; Rodríguez et al., 2021), with an analogous pattern reported for mineral phosphorus (Diao et al., 2023). Particles deposited during the dissipation phase therefore contribute disproportionately to the bioavailable nutrient supply, which is directly relevant for Mediterranean oligotrophic waters, where Saharan dust is a recognised nutrient source. The enrichment of iron-bearing minerals occurs within the finest size fractions (Figure 8), the particles expected to remain airborne longest. This agrees with the reported occurrence of Fe oxide-hydroxides in Saharan dust, predominantly associated with particles smaller than 2 $\mu$m and with the highest mass fraction below 1 $\mu$m (Panta et al., 2023).

https://doi.org/10.5194/egusphere-2026-5232
Preprint. Discussion started: 11 September 2026


### 4.3 Spatiotemporal dynamics and compositional heterogeneity of mediterranean deposition

#### 4.3.1 Contribution of episodic events versus continuous deposition

The five highest-intensity dust episodes account for approximately 20 % of the cumulative dust flux at both sites (Figure 11), and the remaining 80 % is deposited during moderate and low-intensity intervals. The annual mineral budget is therefore dominated by continuous deposition, in contrast to approaches that attribute it mainly to exceptional dry deposition events (Ounissi et al., 2018; Vincent et al., 2016).

Sulfate deposition is more strongly concentrated in these extreme events than mineral dust. The top five events contribute approximately 40 % of the total sulfate flux (Figure 11), following a two-regime structure, a long period of negligible accumulation at low intensities followed by a steep increase confined to the upper tail of the distribution. This behaviour follows the episodic variability of secondary sulfate loading in the Mediterranean, controlled at the synoptic scale by continental air-mass intrusions from Eastern Europe and Turkey that carry secondary inorganic aerosol in the fine fraction (Dimitriou et al., 2022a; Fakhri et al., 2023; Florou et al., 2024), enhanced by $SO_2$ oxidation during prolonged exposure to elevated OH concentrations over the sea (Bettineschi et al., 2025), and further modulated by NAO variability and synoptic blocking (Dayan, 2023a; Nabat et al., 2020).

The timing of the sulfate maximum also differs between the two sites. The peak occurs in April at San Lawrenz and in June–July at Lecce (Figure 10), a divergence that reflects the different source regions to which each site is exposed. San Lawrenz, mainly exposed to westerly flows that carry anthropogenic fine aerosol from Western Europe (Cerro et al., 2020; Dayan, 2023b), records its sulfate maximum in spring, when higher solar radiation raises hydroxyl radical concentrations and accelerates $SO_2$ oxidation over the sea before the air masses reach the site (Bettineschi et al., 2025; Gong et al., 2022; Yang et al., 2024).

Lecce, approximately 13 km from the Adriatic coast (Donateo et al., 2023), receives continental flows from the Balkans and from eastern and central Europe, well-documented sources of industrial secondary inorganic aerosol (Casotto et al., 2022; Dimitriou et al., 2022b; Tsagkaraki et al., 2021). Its summer maximum is attributable to enhanced sulfate production during transport, driven by biogenic gaseous precursors of marine origin and oxidation under summer conditions (Argyropoulos et al., 2012).

#### 4.3.2 Multi-dimensional source attribution

Aerosol sources and transport pathways contributing to dry deposition in the central Mediterranean are dynamic and multi-regional (Bitzan et al., 2025; Peccarrisi et al., 2025; Sannino et al., 2022). In the MA-CWT analysis presented, the geographical origin of the deposited material varies with particle class, size fraction, and season, and this variation is reproduced at both sites.

The dependence on particle class is most evident when comparing mineral and anthropogenic components in each location (Figure 14). At Lecce, clay minerals exhibit a broad footprint across northwestern Africa, consistent with aluminosilicate-rich dust from the western Sahara and Maghreb (Párraga et al., 2021; Remoundaki et al., 2011). Sulfates show maxima over the

https://doi.org/10.5194/egusphere-2026-5232
Preprint. Discussion started: 11 September 2026


Balkans and central Europe, and Pb-containing particles resolve a distinct signal over southwestern Europe, in agreement of industrial and traffic-related sources (Radovanović et al., 2025; Traka et al., 2026; Vannini et al., 2021). At San Lawrenz, sulfates shift toward the Iberian Peninsula and northern Africa, clay minerals remain confined to northern Africa, and Pb-containing particles point toward mining activities in northwestern Africa (Ech-Charef et al., 2025; Leila et al., 2021)(Figure 15).

Source regions also differ between size fractions of the same particle class (Figs. S4 and S5). For sea salt at Lecce, the fine fraction reflects nearby Mediterranean sources while the supercoarse fraction shifts progressively toward the North Atlantic. The North Atlantic generates systematically higher sea salt emission rates than the Mediterranean because of its greater fetch and more energetic wave field (Baldasano et al., 2011; Laussac et al., 2018; Martins et al., 2026; Smith et al., 1993), producing an emission spectrum enriched in coarse and supercoarse particles relative to enclosed seas. Under persistent westerly storm conditions, zonal transport can be sufficiently rapid that gravitational settling does not remove the largest particles before they reach the central Mediterranean (Singh et al., 2024). The inland position of Lecce attenuates the local coastal marine signal through size-selective deposition, which makes the Atlantic component detectable there; at San Lawrenz the same signal is masked by the proximal coastline. For clay minerals at Lecce, the fine fraction links to northwestern Africa while the supercoarse fraction extends toward northern Europe, consistent with size-segregation during long-range transport (Alastuey et al., 2004; Almeida et al., 2006; van der Does et al., 2016). The size dependence also appears in the correlations between $PM_{10}$ and deposited mass. Associations improve substantially when restricted to the fine deposited fraction ($<10$ $\mu$m), reaching r = 0.74 at Lecce and r = 0.78 at San Lawrenz, whereas the total deposited records show only moderate correlations. The coarse component integrates several size-segregated source populations with short atmospheric residence times and non-linear deposition behaviour, which a single bulk mass metric cannot resolve.

The source regions also shift with season. Summer dust sources at both sites extend toward Algeria, Tunisia, and Libya, the longest transport ranges in the record, in line with enhanced Saharan convective activity (Coz et al., 2009). In contrast, winter signals become more spatially constrained and site-specific, indicating regional resuspension at Lecce and short-range frontal transport at San Lawrenz, attributable to the absence of the sustained synoptic-scale advection that characterizes summer events (Bencherif et al., 2026; Zheng et al., 2026) (Figure 16). During winter, Lecce exhibits a more complex footprint, likely influenced by local flow modifications and multiple contributing source sectors, as further discussed in Section 4.4.1. This seasonality implies that short-duration campaigns sample different source regions depending on when they are conducted, a limitation especially relevant for studies that infer annual deposition budgets from single-season measurements.

#### 4.3.3 Distinguishing Local Carbonate Sources from Saharan Dust using Ca-rich Particles

While other silicates, feldspars, clay minerals, and oxides/hydroxides form a tightly coupled geochemical cluster ($r > 0.7$), Ca-rich particles show only moderate correlation with this primary silicate group (Figure 6), suggesting that a portion of the Ca-rich flux originates from sources operating independently of the main Saharan transport pathway.

The relative abundance of Ca-rich particles also differs between deposition regimes. Ca-rich particles account for 3.6 % of the mineral fraction at Lecce and 18 % at San Lawrenz during peak events, rising to 39 % and 41 % respectively under

https://doi.org/10.5194/egusphere-2026-5232
Preprint. Discussion started: 11 September 2026


background conditions (Figure 5). Absolute Ca-rich deposition remains comparable between regimes; the relative increase arises because the Saharan silicate contribution declines under background conditions, exposing a baseline Ca-rich component that is continuously present but compositionally masked during major intrusions.

The accumulated deposited mass shows the same site contrast. During winter, San Lawrenz records a Ca-rich deposition flux of $3.1 \times 10^3$ mg/m$^2$, compared with $2.5 \times 10^2$ mg/m$^2$ at Lecce, a difference exceeding one order of magnitude that a Saharan origin alone cannot explain, since it persists during summer, when both stations receive aerosols from North Africa. The most plausible explanation is an additional local source at San Lawrenz. This interpretation is in agreement with Scerri et al. (2016), who investigated $PM_{10}$ composition on Gozo Island using elemental analysis and Positive Matrix Factorization (PMF) and identified a local crustal factor, rich in Ca, accounting for approximately 6 % of the $PM_{10}$ mass. Although this contribution may appear small compared with the Ca-rich deposition observed here, the discrepancy is mainly methodological. Scerri et al. focused exclusively on suspended $PM_{10}$, whereas the present study quantifies the full deposited particle spectrum, including particles larger than 10 $\mu$m. This distinction matters because particles larger than 10 $\mu$m account for 87.2 % and 94.9 % of the deposited Ca-rich mass at Lecce and San Lawrenz, respectively, despite representing only 3.9 % and 8.0 % of the corresponding particle number fluxes. The largest particles therefore dominate the Ca-rich deposition flux, which explains why studies restricted to $PM_{10}$ capture only a small fraction of the local contribution.

The geology of the Maltese archipelago supports a local carbonate source. The archipelago is composed predominantly of Globigerina Limestone and other carbonate formations (Faghih et al., 2025; Gauci et al., 2017; Haines et al., 2016; Sammut et al., 2017), lithologies susceptible to mechanical weathering and wind-driven resuspension, particularly during the strong winds and frontal passages of the Mediterranean winter, when Saharan dust transport reaches its seasonal minimum. At San Lawrenz this material is also actively extracted, three open-cast limestone quarries are located approximately 800 m to the SW, S and SE of the sampling site. In addition, marine aerosol enriched in biogenic calcite derived from coccolithophore-rich surface waters (Mukherjee et al., 2020; Skampa et al., 2020) may provide a further source of Ca-rich particles at the coastal San Lawrenz site. No comparable winter enhancement occurs at Lecce; at this inland site the Ca-rich signal is more likely to reflect a regional background influenced by distal Saharan carbonate transport and the resuspension of calcareous soils from southern Italy (Masoumi et al., 2024).

### 4.4 Limitations

First, the sampling protocol resolves episodes but not sub-diurnal variability. Bulk deposition was collected as multi-hour integrated samples, which captures episode-scale dynamics and seasonal patterns. The phase lag between the dust peak and the maximum mixed-fraction proportions documented in Section 4.2 is therefore a sampling-interval-averaged signal; the true transition may be stronger, and its timing cannot be determined from this dataset.

Second, the study period of approximately two years (2017–2018) is sufficient to identify seasonal patterns and characterise the two contrasting aerosol regimes, but insufficient to separate interannual variability from seasonal structure. The Mediterranean is subject to substantial interannual variability in Saharan dust export driven by NAO phase, ENSO influence, and multi-year drought cycles in source regions (Di Biagio et al., 2022; Moulin and Chiapello, 2004; Nakamae and Shiotani,

https://doi.org/10.5194/egusphere-2026-5232
Preprint. Discussion started: 11 September 2026


2013). The seasonal MA-CWT footprints and deposition ratios reported here are therefore representative of the sampling period and not climatological means, and their generalisability should be tested against longer observational records or reanalysis products.

Third, several months within the study period lack samples because of logistical interruptions, and these gaps are not uniformly distributed across seasons. Where missing months are concentrated in a particular season at one site, the derived seasonal averages and annual flux estimates carry a systematic bias that interpolation cannot correct. Annual fluxes and seasonal composites are reported from the available samples only, and comparisons between seasons should be read in light of the differing temporal completeness of each site–season combination.

Finally, the MA-CWT analysis at Lecce shows a comparatively diffuse spatial footprint across multiple particle classes. This pattern may reflect local or regional sources near the receptor that are not fully captured within the backward-trajectory ensemble. Under such conditions, deposition signals associated with source directions poorly represented in the trajectory ensemble are spatially smeared by the CWT algorithm across a broad geographical region instead of being concentrated over the true source area.

## 5 Conclusions

The multi-dimensional framework applied here combines flux measurements, automated single-particle analysis, and class-resolved trajectory-based source attribution, and it resolves compositional structure that bulk mass metrics and single-variable source attribution do not separate. Lecce and San Lawrenz diverge through the interplay between coastal distance and large-scale transport exposure, not through meteorological forcing alone. Sites within the same region can therefore sample different aerosol environments, which constrains the spatial extrapolation of deposition estimates across the Mediterranean and the representativeness of single-site monitoring strategies.

Low and moderate deposition rate intervals contribute the greater part of the annual dust budget. This runs against a widely held assumption in Mediterranean deposition research, that annual fluxes are controlled primarily by episodic transport events. Models and observational programmes designed around extreme events will therefore misrepresent the integrated annual budget, particularly for the fine fraction, which couples most effectively with atmospheric PM and carries the largest anthropogenic and secondary signals.

The phase lag between dust concentration peaks and the maximum relative abundance of mixed silicate-sulfate and silicate-sea-salt particles identifies atmospheric aging as an active and quantifiable process operating on the timescale of individual Saharan intrusions. Iron solubility and phosphorus bioavailability increase during this aging phase, so the biogeochemical impact of a dust event on Mediterranean surface waters is offset in time from its mass peak. Bulk deposition approaches do not resolve this offset, which affects nutrient flux estimates to oligotrophic ecosystems.

Finally, Ca-rich particles function as a geochemical tracer for the balance between long-range Saharan transport and local carbonate sources, a balance that shifts seasonally and that become detectable once the Saharan silicate overprint is resolved and removed analytically. Locally derived mineral aerosol of this kind is likely to be overlooked in source-attribution studies

https://doi.org/10.5194/egusphere-2026-5232
Preprint. Discussion started: 11 September 2026


focused on long-range transport. Extending this framework to the full XMed-Dry network and to longer observational records would allow the interannual variability of these patterns, driven by NAO phase and multi-year changes in Saharan dust export, to be assessed, and would provide stronger observational constraints for dry deposition parameterisations in regional climate and atmospheric chemistry models.

*Code and data availability.* The measurement data underlying this work are archived in the Zenodo repository at https://doi.org/10.5281/zenodo.22146888 (Morán et al., 2026). For every particle analysed at Lecce and San Lawrenz they give the elemental composition in atomic percent, the volume-equivalent diameter, the dry mass, the number and mass deposition fluxes and rates, and the assigned particle class and group. Their mixing state is reported as pure or internally mixed silicate, sulfate, sea salt and other components. The $PM_{10}$ concentrations at Arnesano-Riesci and Gharb and the wind direction and speed at the CNR ISAC micrometeorological station and at Gharb are archived for 2017–2018. Every variable is defined with its unit.

ERA5 is distributed by the Copernicus Climate Change Service (Hersbach et al., 2017; Copernicus Climate Change Service, 2023) and the CAMS European air quality reanalysis by the Copernicus Atmosphere Data Store (Copernicus Atmosphere Monitoring Service, 2021; Institut national de l'environnement industriel et des risques et al., 2022).

*Author contributions.* Marcos Morán: conceptualization, data curation, formal analysis, investigation, methodology, software, validation, visualization, writing – original draft preparation, writing – review and editing. Kilian Schneiders: investigation, methodology, validation. Melanie Eknayan: investigation. Ferdinando De Tomasi: investigation, writing – review and editing. Pierina Ielpo: investigation, resources, writing – review and editing. Mark Scerri: investigation, writing – review and editing. Michael Nolle: investigation, resources, writing – review and editing. Konrad Kandler: conceptualization, data curation, funding acquisition, investigation, project administration, software, supervision, validation, writing – review and editing.

*Competing interests.* The authors declare that they have no conflict of interest.

*Acknowledgements.* We thank Dr. Paolo Martano for providing the local meteorological data from the CNR-ISAC Micrometeorological Station in Lecce, which he manages. We acknowledge the Agenzia Regionale per la Prevenzione e Protezione dell'Ambiente Puglia (ARPA Puglia) and the Environment and Resources Authority (ERA), Malta, for making available the air quality monitoring data from the Arnesano-Riesci and Gharb stations. We also thank the XMed-Dry network partners for the coordination of the sampling campaign. This publication was generated using Copernicus Climate Change Service and Copernicus Atmosphere Monitoring Service information. Neither the European Commission nor ECMWF is responsible for any use that may be made of the Copernicus information or data it contains.

https://doi.org/10.5194/egusphere-2026-5232
Preprint. Discussion started: 11 September 2026


*Financial support.* This study was supported by funding from the European Union's Horizon Europe Research and Innovation Programme under the Marie Skłodowska-Curie grant agreement No. 101168425 (Dust-DN).

https://doi.org/10.5194/egusphere-2026-5232
Preprint. Discussion started: 11 September 2026


## References

Adame, J. A., Notario, A., Cuevas, C. A., and Saiz-Lopez, A.: Saharan air outflow variability in the 1980–2020 period, Science of The Total Environment, 839, 156 268, https://doi.org/10.1016/j.scitotenv.2022.156268, 2022.

Alastuey, A., Querol, X., Rodríguez, S., Plana, F., Lopez-Soler, A., Ruiz, C., and Mantilla, E.: Monitoring of atmospheric particulate matter around sources of secondary inorganic aerosol, Atmospheric Environment, 38, 4979–4992, https://doi.org/10.1016/j.atmosenv.2004.06.026, 2004.

Almeida, S. M., Pio, C. A., Freitas, M. C., Reis, M. A., and Trancoso, M. A.: Approaching PM2.5 and PM2.5 - 10 source apportionment by mass balance analysis, principal component analysis and particle size distribution, Science of The Total Environment, 368, 663–674, https://doi.org/10.1016/j.scitotenv.2006.03.031, 2006.

Argyropoulos, G., Manoli, E., Kouras, A., and Samara, C.: Concentrations and source apportionment of PM10 and associated major and trace elements in the Rhodes Island, Greece, Science of The Total Environment, 432, 12–22, https://doi.org/10.1016/j.scitotenv.2012.05.076, 2012.

Aryasree, S., Kandler, K., Benker, N., Walser, A., Tipka, A., Dollner, M., Seibert, P., and Weinzierl, B.: Vertical Variability in morphology, chemistry and optical properties of the transported Saharan air layer measured from Cape Verde and the Caribbean, Royal Society Open Science, 11, 231 433, https://doi.org/10.1098/rsos.231433, 2024.

Axson, J. L., Shen, H., Bondy, A. L., Landry, C. C., Welz, J., Creamean, J. M., and Ault, A. P.: Transported Mineral Dust Deposition Case Study at a Hydrologically Sensitive Mountain Site: Size and Composition Shifts in Ambient Aerosol and Snowpack, Aerosol and Air Quality Research, 16, 555–567, https://doi.org/10.4209/aaqr.2015.05.0346, 2016.

Bakels, L., Tatsii, D., Tipka, A., Thompson, R., Dütsch, M., Blaschek, M., Seibert, P., Baier, K., Bucci, S., Cassiani, M., Eckhardt, S., Groot Zwaaftink, C., Henne, S., Kaufmann, P., Lechner, V., Maurer, C., Mulder, M. D., Pisso, I., Plach, A., and Stohl, A.: FLEXPART version 11: Improved accuracy, efficiency, and flexibility, Geoscientific Model Development, 17, 7595–7627, https://doi.org/10.5194/gmd-17-7595-2024, 2024.

Baldasano, J. M., Pay, M. T., Jorba, O., Gassó, S., and Jiménez-Guerrero, P.: An annual assessment of air quality with the CALIOPE modeling system over Spain, Science of The Total Environment, 409, 2163–2178, https://doi.org/10.1016/j.scitotenv.2011.01.041, 2011.

Becagli, S.: Aerosol Composition and Reactivity, in: Atmospheric Chemistry in the Mediterranean Region: Volume 2–From Air Pollutant Sources to Impacts, edited by Dulac, F., Sauvage, S., and Hamonou, E., pp. 227–251, Springer International Publishing, https://doi.org/10.1007/978-3-030-82385-6_13, 2022.

Bencherif, H., Koutoumboga, B., Bounhir, A., Millet, T., Ranaivombola, M., Bègue, N., Guedouali, F., and Mellouki, A.: Study of Saharan dust events in Southern Morocco using ground-based observations (2004-2022), Remote Sensing Applications: Society and Environment, 42, 101 977, https://doi.org/10.1016/j.rsase.2026.101977, 2026.

Bettineschi, M., Vitali, B., Cholakian, A., Zardi, D., Bianchi, F., Sinclair, V., Mikkola, J., Cristofanelli, P., Marinoni, A., Mazzini, M., Heikkinen, L., Aurela, M., Paglione, M., Bessagnet, B., Tuccella, P., and Ciarelli, G.: Across land, sea, and mountains: Sulphate aerosol sources and transport dynamics over the northern Apennines, Environmental Science: Atmospheres, 5, 1023–1034, https://doi.org/10.1039/D5EA00035A, 2025.

Bibi, M., Saad, M., Masmoudi, M., Laurent, B., and Alfaro, S. C.: Long-term (1980–2018) spatial and temporal variability of the atmospheric dust load and deposition fluxes along the North-African coast of the Mediterranean Sea, Atmospheric Research, 234, 104 689, https://doi.org/10.1016/j.atmosres.2019.104689, 2020.

https://doi.org/10.5194/egusphere-2026-5232
Preprint. Discussion started: 11 September 2026


Bitzan, S., Kirsten, F., Christidis, G. E., Makri, P., and Schepanski, K.: Spatial and temporal variability of surface dust concentration in western Crete (Greece) – Development of a monitoring network, Aeolian Research, 74, 101 005, https://doi.org/10.1016/j.aeolia.2025.101005, 2025.

Bruch, W., Piazzola, J., Branger, H., van Eijk, A. M. J., Luneau, C., Bourras, D., and Tedeschi, G.: Sea-Spray-Generation Dependence on Wind and Wave Combinations: A Laboratory Study, Boundary-Layer Meteorology, 180, 477–505, https://doi.org/10.1007/s10546-021-00636-y, 2021.

Caggiano, R., Fiore, S., Lettino, A., Macchiato, M., Sabia, S., and Trippetta, S.: PM2.5 measurements in a Mediterranean site: Two typical cases, Atmospheric Research, 102, 157–166, https://doi.org/10.1016/j.atmosres.2011.06.015, 2011.

Casotto, R., Cvitešić Kušan, A., Bhattu, D., Cui, T., Manousakas, M. I., Frka, S., Kroflič, A., Grgić, I., Ciglenečki, I., Baltensperger, U., Slowik, J. G., Daellenbach, K. R., and Prévôt, A. S. H.: Chemical composition and sources of organic aerosol on the Adriatic coast in Croatia, Atmospheric Environment: X, 13, 100 159, https://doi.org/10.1016/j.aeaoa.2022.100159, 2022.

Cerro, J. C., Cerdà, V., Querol, X., Alastuey, A., Bujosa, C., and Pey, J.: Variability of air pollutants, and PM composition and sources at a regional background site in the Balearic Islands: Review of western Mediterranean phenomenology from a 3-year study, Science of The Total Environment, 717, 137 177, https://doi.org/10.1016/j.scitotenv.2020.137177, 2020.

Cesari, D., De Benedetto, G. E., Bonasoni, P., Busetto, M., Dinoi, A., Merico, E., Chirizzi, D., Cristofanelli, P., Donateo, A., Grasso, F. M., Marinoni, A., Pennetta, A., and Contini, D.: Seasonal variability of PM2.5 and PM10 composition and sources in an urban background site in Southern Italy, Science of The Total Environment, 612, 202–213, https://doi.org/10.1016/j.scitotenv.2017.08.230, 2018.

Chen, Z., Li, H., Shang, H., Liu, X., Guo, F., Liu, X., Yu, L., Zhou, B., Liu, X., Shi, Y., Zhang, L., and Ai, Z.: Oxalate-Promoted SO2 Uptake and Oxidation on Iron Minerals: Implications for Secondary Sulfate Aerosol Formation, Environmental Science & Technology, 57, 13 559–13 568, https://doi.org/10.1021/acs.est.3c03369, 2023.

Cheng, I., Zhang, L., Blanchard, P., Dalziel, J., and Tordon, R.: Concentration-weighted trajectory approach to identifying potential sources of speciated atmospheric mercury at an urban coastal site in Nova Scotia, Canada, Atmospheric Chemistry and Physics, 13, 6031–6048, https://doi.org/10.5194/acp-13-6031-2013, 2013.

Chiapello, I., Formenti, P., Mbemba Kabuiku, L., Ducos, F., Tanré, D., and Dulac, F.: Aerosol optical properties derived from POLDER-3/PARASOL (2005–2013) over the Western Mediterranean Sea – Part 2: Spatial distribution and temporal variability, Atmospheric Chemistry and Physics, 21, 12 715–12 737, https://doi.org/10.5194/acp-21-12715-2021, 2021.

Connan, O., Pellerin, G., Maro, D., Damay, P., Hébert, D., Roupsard, P., Rozet, M., and Laguionie, P.: Dry deposition velocities of particles on grass: Field experimental data and comparison with models, Journal of Aerosol Science, 126, 58–67, https://doi.org/10.1016/j.jaerosci.2018.08.004, 2018.

Contini, D., Genga, A., Cesari, D., Siciliano, M., Donateo, A., Bove, M. C., and Guascito, M. R.: Characterisation and source apportionment of PM10 in an urban background site in Lecce, Atmospheric Research, 95, 40–54, https://doi.org/10.1016/j.atmosres.2009.07.010, 2010.

Copernicus Atmosphere Monitoring Service: CAMS European air quality reanalyses, https://doi.org/10.24381/7cc0465a, accessed on 15 August 2025, 2021.

Copernicus Climate Change Service: Complete ERA5 global atmospheric reanalysis, https://doi.org/10.24381/cds.143582cf, accessed on 15 August 2025, 2023.

Coz, E., Gómez-Moreno, F. J., Pujadas, M., Casuccio, G. S., Lersch, T. L., and Artíñano, B.: Individual particle characteristics of North African dust under different long-range transport scenarios, Atmospheric Environment, 43, 1850–1863, https://doi.org/10.1016/j.atmosenv.2008.12.045, 2009.

https://doi.org/10.5194/egusphere-2026-5232
Preprint. Discussion started: 11 September 2026


Cui, J., Zhou, J., and Yang, H.: Atmospheric inorganic nitrogen in dry deposition to a typical red soil agro-ecosystem in southeastern China, Journal of Environmental Monitoring, 12, 1287–1294, https://doi.org/10.1039/B922042A, 2010.

Dall'Osto, M., Harrison, R. M., Highwood, E. J., O'Dowd, C., Ceburnis, D., Querol, X., and Achterberg, E. P.: Variation of the mixing state of Saharan dust particles with atmospheric transport, Atmospheric Environment, 44, 3135–3146, https://doi.org/10.1016/j.atmosenv.2010.05.030, 2010.

Dall'Osto, M., Santl-Temkiv, T., O'Dowd, C., and Harrison, R. M.: Enrichment of organic nitrogen in primary biological particles during advection over the North Atlantic, Atmospheric Environment, 222, 117 160, https://doi.org/10.1016/j.atmosenv.2019.117160, 2020.

Dayan, U.: Impacts of the NAO on Atmospheric Pollution in the Mediterranean Basin, in: Hydrological, Socioeconomic and Ecological Impacts of the North Atlantic Oscillation in the Mediterranean Region, edited by Vicente-Serrano, S. M. and Trigo, R. M., pp. 171–181, Springer Netherlands, https://doi.org/10.1007/978-94-007-1372-7_12, 2011.

Dayan, U.: General Atmospheric Conditions and Macroscale Processes, in: Atmospheric Chemistry in the Mediterranean Region: Volume 1–Background Information and Pollutant Distribution, edited by Dulac, F., Sauvage, S., and Hamonou, E., pp. 101–112, Springer International Publishing, https://doi.org/10.1007/978-3-031-12741-0_5, 2023a.

Dayan, U.: Long-Range and Vertical Transport, Troposphere–Stratosphere Exchange, in: Atmospheric Chemistry in the Mediterranean Region: Volume 1–Background Information and Pollutant Distribution, edited by Dulac, F., Sauvage, S., and Hamonou, E., pp. 127–141, Springer International Publishing, https://doi.org/10.1007/978-3-031-12741-0_7, 2023b.

Deike, L.: Mass Transfer at the Ocean–Atmosphere Interface: The Role of Wave Breaking, Droplets, and Bubbles, Annual Review of Fluid Mechanics, 54, 191–224, https://doi.org/10.1146/annurev-fluid-030121-014132, 2022.

Deike, L., Reichl, B. G., and Paulot, F.: A Mechanistic Sea Spray Generation Function Based on the Sea State and the Physics of Bubble Bursting, AGU Advances, 3, https://doi.org/10.1029/2022AV000750, 2022.

Di Biagio, C., Banks, J. R., and Gaetani, M.: 7.11–Dust Atmospheric Transport Over Long Distances, in: Treatise on Geomorphology (Second Edition), edited by Shroder, J. F., pp. 259–300, Academic Press, https://doi.org/10.1016/B978-0-12-818234-5.00033-X, 2022.

Di Gilio, A., de Gennaro, G., Dambruoso, P., and Ventrella, G.: An integrated approach using high time-resolved tools to study the origin of aerosols, Science of The Total Environment, 530–531, 28–37, https://doi.org/10.1016/j.scitotenv.2015.04.073, 2015.

Diao, X., Widory, D., Ram, K., Tripathee, L., Bikkina, S., Kawamura, K., Gao, S., Wan, X., Wu, G., Pei, Q., Wang, X., and Cong, Z.: Atmospheric phosphorus and its geochemical cycling: Fundamentals, progress, and perspectives, Earth-Science Reviews, 243, 104 492, https://doi.org/10.1016/j.earscirev.2023.104492, 2023.

Dimitriou, K., Pikridas, M., Oikonomou, K., Sciare, J., Savvides, C., Vassiliadou, E., and Mihalopoulos, N.: A 3-Dimensional analysis of long-range transported particulate matter to the Eastern Mediterranean: Implication for the chemical components of PM1 and PM10, Atmospheric Pollution Research, 13, 101 485, https://doi.org/10.1016/j.apr.2022.101485, 2022a.

Dimitriou, K., Tsagkaraki, M., Zarmpas, P., and Mihalopoulos, N.: Impact of spatial and vertical distribution of air masses on PM10 chemical components at the Eastern Mediterranean – A seasonal approach, Atmospheric Research, 266, 105 974, https://doi.org/10.1016/j.atmosres.2021.105974, 2022b.

Donateo, A., Palusci, O., Pappaccogli, G., Esposito, A., Martilli, A., Santiago, J. L., and Buccolieri, R.: Analysis of urban heat island and human thermal comfort in a Mediterranean city: A case study of Lecce (Italy), Sustainable Cities and Society, 98, 104 849, https://doi.org/10.1016/j.scs.2023.104849, 2023.

Dulac, F., Mihalopoulos, N., Kaskaoutis, D. G., Querol, X., di Sarra, A., Masson, O., Pey, J., Sciare, J., and Sicard, M.: History of Mediterranean Aerosol Observations, in: Atmospheric Chemistry in the Mediterranean Region: Volume 1–Background Informa-

https://doi.org/10.5194/egusphere-2026-5232
Preprint. Discussion started: 11 September 2026


tion and Pollutant Distribution, edited by Dulac, F., Sauvage, S., and Hamonou, E., pp. 145–252, Springer International Publishing, https://doi.org/10.1007/978-3-031-12741-0_8, 2023.

Ech-Charef, A., EL Houfy, F. Z., Dekayir, A., Jordan, G., Labaioui, A., Rouai, M., and EL Alaoui, L.: Potentially Toxic elements (PTEs) contamination and human health risk assessment of soils in the vicinity of the abandoned lead mine of Zeïda, Upper Moulouya basin in Morocco, Journal of African Earth Sciences, 230, 105 731, https://doi.org/10.1016/j.jafrearsci.2025.105731, 2025.

Efron, B.: Bootstrap Methods: Another Look at the Jackknife, The Annals of Statistics, 7, 1–26, https://doi.org/10.1214/aos/1176344552, 1979.

Emerson, E. W., Hodshire, A. L., DeBolt, H. M., Bilsback, K. R., Pierce, J. R., McMeeking, G. R., and Farmer, D. K.: Revisiting particle dry deposition and its role in radiative effect estimates, Proceedings of the National Academy of Sciences, 117, 26 076–26 082, https://doi.org/10.1073/pnas.2014761117, 2020.

Faghih, Z., Haroon, A., Jegen, M., Berndt, C., Gehrmann, R., Schwalenberg, K., Schmidt, M., Müller, T., and Weymer, B. A.: Investigation of offshore freshened groundwater using marine controlled–source electromagnetic: Insights from Gozo, Maltese Islands, Journal of Applied Geophysics, 241, 105 842, https://doi.org/10.1016/j.jappgeo.2025.105842, 2025.

Fakhri, N., Fadel, M., Öztürk, F., Keleş, M., Iakovides, M., Pikridas, M., Abdallah, C., Karam, C., Sciare, J., Hayes, P. L., and Afif, C.: Comprehensive chemical characterization of PM2.5 in the large East Mediterranean-Middle East city of Beirut, Lebanon, Journal of Environmental Sciences, 133, 118–137, https://doi.org/10.1016/j.jes.2022.07.010, 2023.

Farmer, D. K. and Riches, M.: Measuring Biosphere–Atmosphere Exchange of Short-Lived Climate Forcers and Their Precursors, Accounts of Chemical Research, 53, 1427–1435, https://doi.org/10.1021/acs.accounts.0c00203, 2020.

Farmer, D. K., Boedicker, E. K., and DeBolt, H. M.: Dry Deposition of Atmospheric Aerosols: Approaches, Observations, and Mechanisms, Annual Review of Physical Chemistry, 72, 375–397, https://doi.org/10.1146/annurev-physchem-090519-034936, 2021.

Flores, J. M., Bourdin, G., Kostinski, A. B., Altaratz, O., Dagan, G., Lombard, F., Haëntjens, N., Boss, E., Sullivan, M. B., Gorsky, G., Lang-Yona, N., Trainic, M., Romac, S., Voolstra, C. R., Rudich, Y., Vardi, A., and Koren, I.: Diel cycle of sea spray aerosol concentration, Nature Communications, 12, 5476, https://doi.org/10.1038/s41467-021-25579-3, 2021.

Florou, K., Liangou, A., Kaltsonoudis, C., Louvaris, E., Tasoglou, A., Patoulias, D., Kouvarakis, G., Kalivitis, N., Kourtchev, I., Kalberer, M., Tsagkaraki, M., Mihalopoulos, N., and Pandis, S. N.: Chemical characterization and sources of background aerosols in the eastern Mediterranean, Atmospheric Environment, 324, 120 423, https://doi.org/10.1016/j.atmosenv.2024.120423, 2024.

Floutsi, A. A., Korras-Carraca, M. B., Matsoukas, C., Hatzianastassiou, N., and Biskos, G.: Climatology and trends of aerosol optical depth over the Mediterranean basin during the last 12 years (2002–2014) based on Collection 006 MODIS-Aqua data, Science of The Total Environment, 551–552, 292–303, https://doi.org/10.1016/j.scitotenv.2016.01.192, 2016.

Gauci, R., Schembri, J. A., and Inkpen, R.: Traditional Use of Shore Platforms: A Study of the Artisanal Management of Salinas on the Maltese Islands (Central Mediterranean), Sage Open, 7, 2158244017706 597, https://doi.org/10.1177/2158244017706597, 2017.

Gong, C., Yuan, X., Xing, D., Zhang, D., Martins-Costa, M. T. C., Anglada, J. M., Ruiz-López, M. F., Francisco, J. S., and Zhang, X.: Fast Sulfate Formation Initiated by the Spin-Forbidden Excitation of SO2 at the Air–Water Interface, Journal of the American Chemical Society, 144, 22 302–22 308, https://doi.org/10.1021/jacs.2c10830, 2022.

Goudie, A. S. and Middleton, N. J.: Saharan dust storms: Nature and consequences, Earth-Science Reviews, 56, 179–204, https://doi.org/10.1016/S0012-8252(01, 2001.

Haines, T. J., Michie, E. A. H., Neilson, J. E., and Healy, D.: Permeability evolution across carbonate hosted normal fault zones, Marine and Petroleum Geology, 72, 62–82, https://doi.org/10.1016/j.marpetgeo.2016.01.008, 2016.

https://doi.org/10.5194/egusphere-2026-5232
Preprint. Discussion started: 11 September 2026


Hersbach, H., Bell, B., Berrisford, P., Hirahara, S., Horányi, A., Muñoz Sabater, J., Nicolas, J., Peubey, C., Radu, R., Schepers, D., Simmons, A., Soci, C., Abdalla, S., Abellan, X., Balsamo, G., Bechtold, P., Biavati, G., Bidlot, J., Bonavita, M., De Chiara, G., Dahlgren, P., Dee, D., Diamantakis, M., Dragani, R., Flemming, J., Forbes, R., Fuentes, M., Geer, A., Haimberger, L., Healy, S., Hogan, R. J., Hólm, E., Janisková, M., Keeley, S., Laloyaux, P., Lopez, P., Lupu, C., Radnoti, G., de Rosnay, P., Rozum, I., Vamborg, F., Villaume, S., and Thépaut, J.-N.: Complete ERA5 from 1940: Fifth generation of ECMWF atmospheric reanalyses of the global climate, https://doi.org/10.24381/cds.143582cf, accessed on 15 August 2025, 2017.

Hersbach, H., Bell, B., Berrisford, P., Hirahara, S., Horányi, A., Muñoz-Sabater, J., Nicolas, J., Peubey, C., Radu, R., Schepers, D., Simmons, A., Soci, C., Abdalla, S., Abellan, X., Balsamo, G., Bechtold, P., Biavati, G., Bidlot, J., Bonavita, M., and Thépaut, J.-N.: The ERA5 global reanalysis, Quarterly Journal of the Royal Meteorological Society, 146, 1999–2049, https://doi.org/10.1002/qj.3803, 2020.

Institut national de l'environnement industriel et des risques, Aarhus University, Norwegian Meteorological Institute (MET Norway), Jülich Institut für Energie- und Klimaforschung (IEK), Institute of Environmental Protection – National Research Institute (IEP-NRI), Koninklijk Nederlands Meteorologisch Instituut (KNMI), METEO FRANCE, Nederlandse Organisatie voor toegepast-natuurwetenschappelijk onderzoek (TNO), Swedish Meteorological and Hydrological Institute (SMHI), Finnish Meteorological Institute (FMI), Italian National Agency for New Technologies, Energy and Sustainable Economic Development (ENEA), and Barcelona Supercomputing Center (BSC): CAMS European air quality forecasts, ENSEMBLE data, https://ads.atmosphere.copernicus.eu/datasets/cams-europe-air-quality-reanalyses, accessed on 15 August 2025, 2022.

Jeong, U., Kim, J., Lee, H., Jung, J., Kim, Y. J., Song, C. H., and Koo, J.-H.: Estimation of the contributions of long range transported aerosol in East Asia to carbonaceous aerosol and PM concentrations in Seoul, Korea using highly time resolved measurements: A PSCF model approach, Journal of Environmental Monitoring, 13, 1905–1918, https://doi.org/10.1039/C0EM00659A, 2011.

Kabashnikov, V. P., Chaikovsky, A. P., Kucsera, T. L., and Metelskaya, N. S.: Estimated accuracy of three common trajectory statistical methods, Atmospheric Environment, 45, 5425–5430, https://doi.org/10.1016/j.atmosenv.2011.07.006, 2011.

Kandler, K., SchüTZ, L., Deutscher, C., Ebert, M., Hofmann, H., JäCKEL, S., Jaenicke, R., Knippertz, P., Lieke, K., Massling, A., Petzold, A., Schladitz, A., Weinzierl, B., Wiedensohler, A., Zorn, S., and Weinbruch1, S.: Size distribution, mass concentration, chemical and mineralogical composition and derived optical parameters of the boundary layer aerosol at Tinfou, Morocco, during SAMUM 2006, Tellus B: Chemical and Physical Meteorology, 61, 32–50, https://doi.org/10.1111/j.1600-0889.2008.00385.x, 2009.

Kandler, K., De La Rosa, J., Torressánchez, R., Aviles, M., M Sánchez De La Campa, A., Alastuey, A., Perez, N., Reche, C., Querol, X., Loyepilot, M., Scerri, M., Nolle, M., Ielpo, P., Eleftheriadis, K., Vassilatou, V., Stavroulas, I., Pikridas, M., Maisser, A., and Dirsch, T.: XMed-Dry - A Cross-Mediterranean Dry Deposition Measurement Network: First results, https://iris.cnr.it/handle/20.500.14243/375099, 2018a.

Kandler, K., Schneiders, K., Ebert, M., Hartmann, M., Weinbruch, S., Prass, M., and Pöhlker, C.: Composition and mixing state of atmospheric aerosols determined by electron microscopy: Method development and application to aged Saharan dust deposition in the Caribbean boundary layer, Atmospheric Chemistry and Physics, 18, 13 429–13 455, https://doi.org/10.5194/acp-18-13429-2018, 2018b.

Kandler, K., Schneiders, K., Heuser, J., Waza, A., Aryasree, S., Althausen, D., Hofer, J., Abdullaev, S. F., and Makhmudov, A. N.: Differences and Similarities of Central Asian, African, and Arctic Dust Composition from a Single Particle Perspective, Atmosphere, 11, https://doi.org/10.3390/atmos11030269, 2020.

Kaskaoutis, D. G., Liakakou, E., Grivas, G., Gerasopoulos, E., Mihalopoulos, N., Alastuey, A., Dulac, F., Pandolfi, M., Sciare, J., and Titos, G.: Chemical Composition and Levels of Concentrations of Aerosols in the Mediterranean, in: Atmospheric Chemistry in the

https://doi.org/10.5194/egusphere-2026-5232
Preprint. Discussion started: 11 September 2026


Mediterranean Region: Volume 1–Background Information and Pollutant Distribution, edited by Dulac, F., Sauvage, S., and Hamonou, E., pp. 253–311, Springer International Publishing, https://doi.org/10.1007/978-3-031-12741-0_9, 2023.

Kishcha, P., Nickovic, S., Starobinets, B., di Sarra, A., Udisti, R., Becagli, S., Sferlazzo, D., Bommarito, C., and Alpert, P.: Sea-salt aerosol forecasts compared with daily measurements at the island of Lampedusa (Central Mediterranean), Atmospheric Research, 100, 28–35, https://doi.org/10.1016/j.atmosres.2010.12.021, 2011.

Kost, O. and Stoll, H.: Marine aerosols in coastal areas and their impact on cave drip water – A monitoring study from Northern Spain, Atmospheric Environment, 302, 119 730, https://doi.org/10.1016/j.atmosenv.2023.119730, 2023.

Koçak, M., Mihalopoulos, N., and Kubilay, N.: Chemical composition of the fine and coarse fraction of aerosols in the northeastern Mediterranean, Atmospheric Environment, 41, 7351–7368, https://doi.org/10.1016/j.atmosenv.2007.05.011, 2007.

Laussac, S., Piazzola, J., Tedeschi, G., Yohia, C., Canepa, E., Rizza, U., and Van Eijk, A. M. J.: Development of a fetch dependent sea-spray source function using aerosol concentration measurements in the North-Western Mediterranean, Atmospheric Environment, 193, 177–189, https://doi.org/10.1016/j.atmosenv.2018.09.009, 2018.

Leila, B., Loubna, B., and Ali, B.: Impacts of mining activities on soil properties: Case studies from Morocco mine sites, Soil Science Annual, 71, 395–407, https://doi.org/10.37501/soilsa/133011, 2021.

Li, J., Wang, Z., Zhuang, G., Luo, G., Sun, Y., and Wang, Q.: Mixing of Asian mineral dust with anthropogenic pollutants over East Asia: A model case study of a super-duststorm in March 2010, Atmospheric Chemistry and Physics, 12, 7591–7607, https://doi.org/10.5194/acp-12-7591-2012, 2012.

Li, R., Jia, X., Wang, F., Ren, Y., Wang, X., Zhang, H., Li, G., Wang, X., and Tang, M.: Heterogeneous reaction of NO2 with hematite, goethite and magnetite: Implications for nitrate formation and iron solubility enhancement, Chemosphere, 242, 125 273, https://doi.org/10.1016/j.chemosphere.2019.125273, 2020.

Li, Z., Guo, J., Ding, A., Liao, H., Liu, J., Sun, Y., Wang, T., Xue, H., Zhang, H., and Zhu, B.: Aerosol and boundary-layer interactions and impact on air quality, National Science Review, 4, 810–833, https://doi.org/10.1093/nsr/nwx117, 2017.

Liang, L., Han, Z., Li, J., Xia, X., Sun, Y., Liao, H., Liu, R., Liang, M., Gao, Y., and Zhang, R.: Emission, transport, deposition, chemical and radiative impacts of mineral dust during severe dust storm periods in March 2021 over East Asia, Science of The Total Environment, 852, 158 459, https://doi.org/10.1016/j.scitotenv.2022.158459, 2022.

Lin, M., Malyshev, S., Shevliakova, E., Paulot, F., Horowitz, L. W., Fares, S., Mikkelsen, T. N., and Zhang, L.: Sensitivity of Ozone Dry Deposition to Ecosystem-Atmosphere Interactions: A Critical Appraisal of Observations and Simulations, Global Biogeochemical Cycles, 33, 1264–1288, https://doi.org/10.1029/2018GB006157, 2019.

Liora, N., Markakis, K., Poupkou, A., Giannaros, T. M., and Melas, D.: The natural emissions model (NEMO): Description, application and model evaluation, Atmospheric Environment, 122, 493–504, https://doi.org/10.1016/j.atmosenv.2015.10.014, 2015.

Liu, D., Taylor, J. W., Crosier, J., Marsden, N., Bower, K. N., Lloyd, G., Ryder, C. L., Brooke, J. K., Cotton, R., Marenco, F., Blyth, A., Cui, Z., Estelles, V., Gallagher, M., Coe, H., and Choularton, T. W.: Aircraft and ground measurements of dust aerosols over the west African coast in summer 2015 during ICE-D and AER-D, Atmospheric Chemistry and Physics, 18, 3817–3838, https://doi.org/10.5194/acp-18-3817-2018, 2018.

Ma, Y., Zhang, X., Xin, J., Zhang, W., Wang, Z., Liu, Q., Wu, F., Wang, L., Lyu, Y., Wang, Q., and Ma, Y.: Mass and number concentration distribution of marine aerosol in the Western Pacific and the influence of continental transport, Environmental Pollution, 298, 118 827, https://doi.org/10.1016/j.envpol.2022.118827, 2022.

https://doi.org/10.5194/egusphere-2026-5232
Preprint. Discussion started: 11 September 2026


Ma, Y., Xin, J., Tian, Y., Yue, C., Zhou, X., Ren, Y., Hao, F., Wang, P., Xie, F., Ren, X., Zhao, D., Wu, L., Pan, X., and Wang, Z.: The interactions of aerosol and planetary boundary layer over a large city in the Mongolian Plateau, Science of The Total Environment, 907, 167 985, https://doi.org/10.1016/j.scitotenv.2023.167985, 2024.

Mahowald, N. M., Scanza, R., Brahney, J., Goodale, C. L., Hess, P. G., Moore, J. K., and Neff, J.: Aerosol Deposition Impacts on Land and Ocean Carbon Cycles, Current Climate Change Reports, 3, 16–31, https://doi.org/10.1007/s40641-017-0056-z, 2017.

Martins, V., Batalha, G., Garcia, F., Gonçalves, C., Lucarelli, F., Alves, C. A., Samek, L., and Almeida, S. M.: Assessing urban air quality in the context of strict traffic restrictions: Particulate matter concentrations, chemical composition and sources, Environmental Pollution, 400, 128 199, https://doi.org/10.1016/j.envpol.2026.128199, 2026.

Masoumi, I., Maggio, S., De Iaco, S., and Ghezelbash, R.: Spatial multi-criteria approaches for estimating geogenic radon hazard index, Science of The Total Environment, 956, 176 419, https://doi.org/10.1016/j.scitotenv.2024.176419, 2024.

Morán, M., Schneiders, K., Eknayan, M., De Tomasi, F., Ielpo, P., Scerri, M., Nolle, M., and Kandler, K.: Class- and size-resolved dry deposition of atmospheric particles at two central Mediterranean sites (Lecce, Italy and San Lawrenz, Malta), 2017–2018, https://doi.org/10.5281/zenodo.22146888, 2026.

Moulin, C. and Chiapello, I.: Evidence of the control of summer atmospheric transport of African dust over the Atlantic by Sahel sources from TOMS satellites (1979–2000), Geophysical Research Letters, 31, https://doi.org/10.1029/2003GL018931, 2004.

Mukherjee, P., Reinfelder, J. R., and Gao, Y.: Enrichment of calcium in sea spray aerosol in the Arctic summer atmosphere, Marine Chemistry, 227, 103 898, https://doi.org/10.1016/j.marchem.2020.103898, 2020.

Nabat, P., Somot, S., Cassou, C., Mallet, M., Michou, M., Bouniol, D., Decharme, B., Drugé, T., Roehrig, R., and Saint-Martin, D.: Modulation of radiative aerosols effects by atmospheric circulation over the Euro-Mediterranean region, Atmospheric Chemistry and Physics, 20, 8315–8349, https://doi.org/10.5194/acp-20-8315-2020, 2020.

Nakamae, K. and Shiotani, M.: Interannual variability in Saharan dust over the North Atlantic Ocean and its relation to meteorological fields during northern winter, Atmospheric Research, 122, 336–346, https://doi.org/10.1016/j.atmosres.2012.09.012, 2013.

Okabe, A., Boots, B. N., and Sugihara, K.: Spatial Tessellations: Concepts and Applications of Voronoi Diagrams, Wiley & Sons, 1992.

Ott, D. K., Cyrs, W., and Peters, T. M.: Passive measurement of coarse particulate matter,, Journal of Aerosol Science, 39, 156–167, https://doi.org/10.1016/j.jaerosci.2007.11.002, 2008.

Ounissi, M., Amira, A. B., and Dulac, F.: Riverine and wet atmospheric inputs of materials to a North Africa coastal site (Annaba Bay, Algeria), Progress in Oceanography, 165, 19–34, https://doi.org/10.1016/j.pocean.2018.04.001, 2018.

Pacyna, J. M.: Atmospheric Deposition: Five-Volume, Encyclopedia of Ecology, https://doi.org/10.1016/B978-008045405-4.00258-5, 2008.

Panta, A., Kandler, K., Alastuey, A., González-Flórez, C., González-Romero, A., Klose, M., Querol, X., Reche, C., Yus-Díez, J., and Pérez García-Pando, C.: Insights into the single-particle composition, size, mixing state, and aspect ratio of freshly emitted mineral dust from field measurements in the Moroccan Sahara using electron microscopy, Atmospheric Chemistry and Physics, 23, 3861–3885, https://doi.org/10.5194/acp-23-3861-2023, 2023.

Pay, M. T., Jiménez-Guerrero, P., Jorba, O., Basart, S., Querol, X., Pandolfi, M., and Baldasano, J. M.: Spatio-temporal variability of concentrations and speciation of particulate matter across Spain in the CALIOPE modeling system, Atmospheric Environment, 46, 376–396, https://doi.org/10.1016/j.atmosenv.2011.09.049, 2012.

Peccarrisi, D., Fragola, M., Romano, S., Fanigliulo, F., Carbone, G. G., Maruccio, L., Contini, D., Quarta, G., and Calcagnile, L.: Characterization of atmospheric aerosol and its carbonaceous components at a central Mediterranean site: A multi-method approach using optical, physical, and isotopic techniques, Atmospheric Environment: X, 28, 100 380, https://doi.org/10.1016/j.aeaoa.2025.100380, 2025.

https://doi.org/10.5194/egusphere-2026-5232
Preprint. Discussion started: 11 September 2026


Perron, M. M. G., Proemse, B. C., Strzelec, M., Gault-Ringold, M., Boyd, P. W., Rodriguez, E. S., Paull, B., and Bowie, A. R.: Origin, transport and deposition of aerosol iron to Australian coastal waters, Atmospheric Environment, 228, 117 432, https://doi.org/10.1016/j.atmosenv.2020.117432, 2020.

Perrone, M. R., Tafuro, A. M., and Kinne, S.: Dust layer effects on the atmospheric radiative budget and heating rate profiles, Atmospheric Environment, 59, 344–354, https://doi.org/10.1016/j.atmosenv.2012.06.012, 2012.

Petroselli, C., Crocchianti, S., Moroni, B., Castellini, S., Selvaggi, R., Nava, S., Calzolai, G., Lucarelli, F., and Cappelletti, D.: Disentangling the major source areas for an intense aerosol advection in the Central Mediterranean on the basis of Potential Source Contribution Function modeling of chemical and size distribution measurements, Atmospheric Research, 204, 67–77, https://doi.org/10.1016/j.atmosres.2018.01.011, 2018.

Párraga, J., Martín-García, J. M., Delgado, G., Molinero-García, A., Cervera-Mata, A., Guerra, I., Fernández-González, M. V., Martín-Rodríguez, F. J., Lyamani, H., Casquero-Vera, J. A., Valenzuela, A., Olmo, F. J., and Delgado, R.: Intrusions of dust and iberulites in Granada basin (Southern Iberian Peninsula). Genesis and formation of atmospheric iberulites, Atmospheric Research, 248, 105 260, https://doi.org/10.1016/j.atmosres.2020.105260, 2021.

Radovanović, M., Filipović, S., and Šimić, G.: When energy resources, transit routes, critical minerals and the interests of great powers meet in the Western Balkans: Do citizens have a voice, Energy Research & Social Science, 126, 104 153, https://doi.org/10.1016/j.erss.2025.104153, 2025.

Remoundaki, E., Bourliva, A., Kokkalis, P., Mamouri, R. E., Papayannis, A., Grigoratos, T., Samara, C., and Tsezos, M.: PM10 composition during an intense Saharan dust transport event over Athens (Greece), Science of The Total Environment, 409, 4361–4372, https://doi.org/10.1016/j.scitotenv.2011.06.026, 2011.

Rizza, U., Kandler, K., Eknayan, M., Passerini, G., Mancinelli, E., Virgili, S., Morichetti, M., Nolle, M., Eleftheriadis, K., Vasilatou, V., and Ielpo, P.: Investigation of an Intense Dust Outbreak in the Mediterranean Using XMed-Dry Network, Multiplatform Observations, and Numerical Modeling, Applied Sciences, 11, 1566, https://doi.org/10.3390/app11041566, 2021.

Rizzo, A., Vandelli, V., Buhagiar, G., Micallef, A. S., and Soldati, M.: Coastal Vulnerability Assessment along the North-Eastern Sector of Gozo Island (Malta, Mediterranean Sea), Water, 12, 1405, https://doi.org/10.3390/w12051405, 2020.

Rodríguez, S., Prospero, J. M., López-Darias, J., García-Alvarez, M.-I., Zuidema, P., Nava, S., Lucarelli, F., Gaston, C. J., Galindo, L., and Sosa, E.: Tracking the changes of iron solubility and air pollutants traces as African dust transits the Atlantic in the Saharan dust outbreaks, Atmospheric Environment, 246, 118 092, https://doi.org/10.1016/j.atmosenv.2020.118092, 2021.

Sammut, S., Gauci, R., Drago, A., Gauci, A., and Azzopardi, J.: Pocket beach sediment: A field investigation of the geodynamic processes of coarse-clastic beaches on the Maltese Islands (Central Mediterranean), Marine Geology, 387, 58–73, https://doi.org/10.1016/j.margeo.2017.02.011, 2017.

Sannino, A., Amoruso, S., Damiano, R., Scollo, S., Sellitto, P., and Boselli, A.: Optical and microphysical characterization of atmospheric aerosol in the Central Mediterranean during simultaneous volcanic ash and desert dust transport events, Atmospheric Research, 271, 106 099, https://doi.org/10.1016/j.atmosres.2022.106099, 2022.

Scerri, M. M., Kandler, K., and Weinbruch, S.: Disentangling the contribution of Saharan dust and marine aerosol to PM10 levels in the Central Mediterranean, Atmospheric Environment, 147, 395–408, https://doi.org/10.1016/j.atmosenv.2016.10.028, 2016.

Schepanski, K., Mallet, M., Heinold, B., and Ulrich, M.: North African dust transport toward the western Mediterranean basin: Atmospheric controls on dust source activation and transport pathways during June–July 2013, Atmospheric Chemistry and Physics, 16, 14 147–14 168, https://doi.org/10.5194/acp-16-14147-2016, 2016.

https://doi.org/10.5194/egusphere-2026-5232
Preprint. Discussion started: 11 September 2026


Shi, Z., Krom, M. D., Jickells, T. D., Bonneville, S., Carslaw, K. S., Mihalopoulos, N., Baker, A. R., and Benning, L. G.: Impacts on iron solubility in the mineral dust by processes in the source region and the atmosphere: A review, Aeolian Research, 5, 21–42, https://doi.org/10.1016/j.aeolia.2012.03.001, 2012.

Shrestha, S., Holz, R. E., Marais, W. J., Buckholtz, Z., Razenkov, I., Eloranta, E., Reid, J. S., Elliott, H. E., Lata, N. N., Cheng, Z., China, S., Blades, E., Ortiz, A. D., Chewitt-Lucas, R., Allen, A., Blades, D., Agrawal, R., Reid, E. A., Ruiz-Plancarte, J., and Gaston, C. J.: Transported African Dust in the Lower Marine Atmospheric Boundary Layer is Internally Mixed with Sea Salt Contributing to Increased Hygroscopicity and a Lower Lidar Depolarization Ratio, Atmospheric Chemistry and Physics, 26, 983–999, https://doi.org/10.5194/acp-26-983-2026, 2026.

Singh, V., Srivastava, A. K., Gupta, A., Konduru, R. T., Singh, A., Singh, S., Kumar, A., Bisht, D. S., and Singh, A. K.: Intensification mechanisms and moisture dynamics of super cyclonic storm 'Amphan' over the Bay of Bengal: Implications for aerosol re-distribution, Science of The Total Environment, 951, 175 501, https://doi.org/10.1016/j.scitotenv.2024.175501, 2024.

Skampa, E., Triantaphyllou, M. V., Dimiza, M. D., Gogou, A., Malinverno, E., Stavrakakis, S., Parinos, C., Panagiotopoulos, I. P., Tselenti, D., Archontikis, O., and Baumann, K.-H.: Coccolithophore export in three deep-sea sites of the Aegean and Ionian Seas (Eastern Mediterranean): Biogeographical patterns and biogenic carbonate fluxes, Deep Sea Research Part II: Topical Studies in Oceanography, Revisiting the Eastern Mediterranean: Recent Knowledge on the Physical, Biogeochemical and Ecosystemic States and Trends (Volume II), 171, 104 690, https://doi.org/10.1016/j.dsr2.2019.104690, 2020.

Smith, M. H., Park, P. M., and Consterdine, I. E.: Marine aerosol concentrations and estimated fluxes over the sea, Quarterly Journal of the Royal Meteorological Society, 119, 809–824, https://doi.org/10.1002/qj.49711951211, 1993.

Sprovieri, F., Bencardino, M., Cofone, F., and Pirrone, N.: Chemical Composition of Aerosol Size Fractions at a Coastal Site in Southwestern Italy: Seasonal Variability and Transport Influence, Journal of the Air & Waste Management Association, 61, 941–951, https://doi.org/10.1080/10473289.2011.599267, 2011.

Sullivan, R. C., Guazzotti, S. A., Sodeman, D. A., and Prather, K. A.: Direct observations of the atmospheric processing of Asian mineral dust, Atmospheric Chemistry and Physics, 7, 1213–1236, https://doi.org/10.5194/acp-7-1213-2007, 2007.

Tedeschi, G. and Piazzola, J.: Development of a 2D marine aerosol transport model: Application to the influence of thermal stability in the marine atmospheric boundary layer, Atmospheric Research, 101, 469–479, https://doi.org/10.1016/j.atmosres.2011.04.013, 2011.

Thiagarajan, V., Nah, T., and Xin, X.: Impacts of atmospheric particulate matter deposition on phytoplankton: A review, Science of The Total Environment, 950, 175 280, https://doi.org/10.1016/j.scitotenv.2024.175280, 2024.

Tian, R., Ma, X., Sha, T., Pan, X., and Wang, Z.: Exploring dust heterogeneous chemistry over China: Insights from field observation and GEOS-Chem simulation, Science of The Total Environment, 798, 149 307, https://doi.org/10.1016/j.scitotenv.2021.149307, 2021.

Tipka, A., Haimberger, L., and Seibert, P.: Flex_extract v7.1.2 – a software package to retrieve and prepare ECMWF data for use in FLEXPART, Geoscientific Model Development, 13, 5277–5310, https://doi.org/10.5194/gmd-13-5277-2020, 2020.

Traka, N., Stergiou, I., Sotiropoulou, R.-E. P., Kaskaoutis, D. G., and Tagaris, E.: A pan-European WRF–CMAQ framework for air quality assessment: Model evaluation and policy baseline, Atmospheric Pollution Research, 17, 102 992, https://doi.org/10.1016/j.apr.2026.102992, 2026.

Tsagkaraki, M., Theodosi, C., Grivas, G., Vargiakaki, E., Sciare, J., Savvides, C., and Mihalopoulos, N.: Spatiotemporal variability and sources of aerosol water-soluble organic nitrogen (WSON), in the Eastern Mediterranean, Atmospheric Environment, 246, 118 144, https://doi.org/10.1016/j.atmosenv.2020.118144, 2021.

https://doi.org/10.5194/egusphere-2026-5232
Preprint. Discussion started: 11 September 2026


Tsamalis, C., Chédin, A., Pelon, J., and Capelle, V.: The seasonal vertical distribution of the Saharan Air Layer and its modulation by the wind, Atmospheric Chemistry and Physics, 13, 11 235–11 257, https://doi.org/10.5194/acp-13-11235-2013, 2013.

van der Does, M., Korte, L. F., Munday, C. I., Brummer, G.-J. A., and Stuut, J.-B. W.: Particle size traces modern Saharan dust transport and deposition across the equatorial North Atlantic, Atmospheric Chemistry and Physics, 16, 13 697–13 710, https://doi.org/10.5194/acp-16-13697-2016, 2016.

Vannini, A., Tedesco, R., Loppi, S., Di Cecco, V., Di Martino, L., Nascimbene, J., Dallo, F., and Barbante, C.: Lichens as monitors of the atmospheric deposition of potentially toxic elements in high elevation Mediterranean ecosystems, Science of The Total Environment, 798, 149 369, https://doi.org/10.1016/j.scitotenv.2021.149369, 2021.

Varenik, A. V. and Konovalov, S. K.: Variations in Concentrations and Ratio of Soluble Forms of Nutrients in Atmospheric Depositions and Effects for Marine Coastal Areas of Crimea, Black Sea, Applied Sciences, 11, 11 509, https://doi.org/10.3390/app112311509, 2021.

Varga, G., Újvári, G., and Kovács, J.: Spatiotemporal patterns of Saharan dust outbreaks in the Mediterranean Basin, Aeolian Research, 15, 151–160, https://doi.org/10.1016/j.aeolia.2014.06.005, 2014.

Vincent, J., Laurent, B., Losno, R., Bon Nguyen, E., Roullet, P., Sauvage, S., Chevaillier, S., Coddeville, P., Ouboulmane, N., di Sarra, A. G., Tovar-Sánchez, A., Sferlazzo, D., Massanet, A., Triquet, S., Morales Baquero, R., Fornier, M., Coursier, C., Desboeufs, K., Dulac, F., and Bergametti, G.: Variability of mineral dust deposition in the western Mediterranean basin and south-east of France, Atmospheric Chemistry and Physics, 16, 8749–8766, https://doi.org/10.5194/acp-16-8749-2016, 2016.

Virtanen, P., Gommers, R., Oliphant, T. E., Haberland, M., Reddy, T., Cournapeau, D., Burovski, E., Peterson, P., Weckesser, W., Bright, J., van der Walt, S. J., Brett, M., Wilson, J., Millman, K. J., Mayorov, N., Nelson, A. R. J., Jones, E., Kern, R., Larson, E., and van Mulbregt, P.: SciPy 1.0: Fundamental algorithms for scientific computing in Python, Nature Methods, 17, 261–272, https://doi.org/10.1038/s41592-019-0686-2, 2020.

Vratolis, S., Diapouli, E., Manousakas, M. I., Almeida, S. M., Beslic, I., Kertesz, Z., Samek, L., and Eleftheriadis, K.: A new method for the quantification of ambient particulate-matter emission fluxes, Atmospheric Chemistry and Physics, 23, 6941–6961, https://doi.org/10.5194/acp-23-6941-2023, 2023.

Waza, A., Schneiders, K., May, J., Rodríguez, S., Epple, B., and Kandler, K.: Field comparison of dry deposition samplers for collection of atmospheric mineral dust: Results from single-particle characterization, Atmospheric Measurement Techniques, 12, 6647–6665, https://doi.org/10.5194/amt-12-6647-2019, 2019.

Wu, M., Liu, X., Zhang, L., Wu, C., Lu, Z., Ma, P.-L., Wang, H., Tilmes, S., Mahowald, N., Matsui, H., and Easter, R. C.: Impacts of Aerosol Dry Deposition on Black Carbon Spatial Distributions and Radiative Effects in the Community Atmosphere Model CAM5, Journal of Advances in Modeling Earth Systems, 10, 1150–1171, https://doi.org/10.1029/2017MS001219, 2018a.

Wu, Y., Liu, J., Zhai, J., Cong, L., Wang, Y., Ma, W., Zhang, Z., and Li, C.: Comparison of dry and wet deposition of particulate matter in near-surface waters during summer, PLOS ONE, 13, e0199 241, https://doi.org/10.1371/journal.pone.0199241, 2018b.

Yang, N., Tsona, N. T., Cheng, S., Li, S., Xu, L., Wang, Y., Wu, L., and Du, L.: Competitive reactions of SO2 and acetic acid on $\alpha$-Al2O3 and CaCO3 particles, Science of The Total Environment, 699, 134 362, https://doi.org/10.1016/j.scitotenv.2019.134362, 2020.

Yang, W., Ma, J., Yang, H., Li, F., and Han, C.: Photoenhanced sulfate formation by the heterogeneous uptake of SO2 on non-photoactive mineral dust, Atmospheric Chemistry and Physics, 24, 6757–6768, https://doi.org/10.5194/acp-24-6757-2024, 2024.

Zheng, J., Yu, H., Zhou, Y., Shi, Y., Zhang, Z., Di Biagio, C., Formenti, P., and Smirnov, A.: A novel retrieval of global dust optical depth and effective diameter based on MODIS thermal infrared observations, Remote Sensing of Environment, 332, 115 083, https://doi.org/10.1016/j.rse.2025.115083, 2026.

https://doi.org/10.5194/egusphere-2026-5232
Preprint. Discussion started: 11 September 2026


Zhou, Y., Gong, S., Zhou, C., Zhang, L., He, J., Wang, Y., Ji, D., Feng, J., Mo, J., and Ke, H.: A new parameterization of uptake coefficients for heterogeneous reactions on multi-component atmospheric aerosols, Science of The Total Environment, 781, 146 372, https://doi.org/10.1016/j.scitotenv.2021.146372, 2021.